Title: Nocturnal aerosol optical depth measurements with modified skyradiometer POM-02 using the moon as a light source

Authors:
Akihiro Uchiyama[1], Masataka Shiobara[2], Hiroshi Kobayashi[3], Tsuneo Matsunaga[1], Akihiro Yamazaki[4], Kazunori Inei[5], Kazuhiro Kawai[5], and Yoshiaki Watanabe[5]

[1] Center for Global Environmental Research, National Institute for Environmental Studies, Tsukuba, Ibaraki 305-8506, Japan
[2] National Institute of Polar Research, Midoricho, Tachikawa, Tokyo 190-8518, Japan
[3] University of Yamanashi, Takeda, Kofu, Yamanashi 400-8510, Japan
[4] Meteorological Research Institute, Japan Meteorological Agency, Tsukuba, Ibaraki 305-0052, Japan
[5] Prede Co., Ltd., Kamidaira, Fussa, Tokyo 197-0012, Japan

Correspondence to: Uchiyama Akihiro (uchiyama.akihiro@nies.go.jp)

Abstract

The majority of aerosol data are obtained from daytime measurements, and there are few datasets available for studying nighttime aerosol characteristics. In order to estimate the aerosol optical depth (AOD) and the precipitable water vapor (PWV) during the nighttime using the moon as a light source, a skyradiometer POM-02 (Prede Ltd., Japan) was modified. The amplifier was adjusted so that POM-02 could measure lower levels of input irradiance. In order to track the moon based on the calculated values, a simplified formula was incorporated into the firmware. A new position sensor with a four-quadrant detector to adjust the tracking of the sun and moon was also developed.

The calibration constant, which is the sensor output for the extra-terrestrial solar and lunar irradiance at the mean earth-sun distance, was determined by using the Langley method. The measurements for the Langley calibration were conducted at the National Oceanic and Atmospheric Administration/Mauna Loa Observatory (NOAA/MLO) from Sep. 28, 2017 to Nov. 7, 2017. By assuming that the correct reflectance is proportional to the reflectance estimated by the Robotic Lunar Observatory (ROLO) irradiance model, the calibration constant for the lunar direct irradiance was successfully determined using the Langley method. The ratio of the

calibration constant for the moon to that for the sun was often greater than 1; the value of the ratio was 0.95 to 1.18 in the visible and near-infrared wavelength region. This indicates that the ROLO model often underestimates the reflectance. In addition, this ratio depended on the phase angle. In this study, this ratio was approximated by a quadratic equation of the phase angle. By using this approximation, the reflectance of the moon can be calculated to within an accuracy of 1% or less.

In order to validate the estimates of the AOD and PWV, continuous measurements with POM-02 were conducted at the Japan Meteorological Agency/Meteorological Research Institute (JMA/MRI) from January 2018 to May 2018, and the AOD and PWV were estimated. The results were compared with the AOD and PWV obtained by independent methods. The AOD was compared with that estimated by the National Institute for Environmental Studies (NIES) High Spectral Resolution Lidar measurements (wavelength: 532 nm), and the PWV was compared with the PWV obtained from a radiosonde and the Global Positioning System. In addition, the continuity of the AOD (PVW) before and after sunrise and sunset in Tsukuba was examined, and the AOD (PWV) of AERONET and that of POM-02 at MLO were compared. In the results, the daytime and nighttime AOD (PWV) measurements are shown to be statistically almost equivalent. The AODs (PWVs) during the daytime and nighttime for POM-02 are presumed to have the same degree of precision and accuracy within the measurement uncertainty.

1. Introduction

Atmospheric aerosols are an important constituent of the atmosphere. Aerosols change the radiation budget directly by absorbing and scattering solar radiation and indirectly through their role as cloud condensation nuclei (CCNs), thereby increasing cloud reflectivity and lifetime (e.g., Ramanathan et al. 2001; Lohmann and Feichter 2005). Aerosols also affect human health as one of the main components of air pollution (Dockery et al. 1993; WHO 2006, 2013).

Atmospheric aerosols have a large variability in time and space. Therefore, measurement networks covering an extensive area on the ground and from space have been developed and established to determine the spatiotemporal distribution of aerosols. Well-known ground-based networks include AERONET (AErosol RObotic NETwork) (Holben et al. 1998), SKYNET (Takamura et al. 2004), and PFR-GAW (Precision Filter Radiometer-Global Atmosphere Watch) (Wehrli 2005). These observation networks use passive radiometers which measure sunlight in the region

from the ultraviolet to shortwave infrared wavelengths and the column average effective aerosol characteristics such as aerosol optical depth (AOD) are retrieved.

Using lidar, which is an active remote sensing instrument, several networks have also been constructed: for example, the Micropulse Lidar Network (MPLNET) by NASA (National Aeronautics and Space Administration) (Welton et al. 2001; Levis et al. 2016), the European Aerosol Research Lidar Network (EARLINET) (Pappalardo et al. 2016) in Europe, the Asian Dust and aerosol lidar observation network (AD-Net) (Shimizu et al. 2017) in East Asia, and the Latin American Lidar Network (LALINET) (Guerrero-Rascado et al. 2016) in South America.

Several satellite programs provide aerosol optical depth data on a global scale: for example, the Moderate Resolution Imaging Spectroradiometer (MODIS) (Remer et al. 2005), Multiangle Imaging Spectroradiometer (MISR) (Kahn et al. 2005), Geostationary Operational Environmental Satellite (GOES) Aerosol Smoke Product (Prados et al. 2007), Sea-viewing Wide Field-of-view Sensor (SeaWiFS) (Wang et al. 2000), Advanced Himawari Imager (AHI) (Yoshida et al. 2018; Kikuchi et al. 2018), and Cloud-Aerosol Lidar and Infrared Pathfinder Satellite Observation (CALIPSO) (Winker et al. 2007).

With the exception of active sensor measurements such as lidar systems, to estimate aerosol characteristics, direct solar irradiance and scattered solar radiance measured with a passive sensor are required. Therefore, the majority of aerosol property data are obtained by daytime measurements, and there are few datasets of nighttime aerosol characteristics available.

To advance the understanding of the diurnal behavior of aerosols, and nocturnal mixing layer dynamics, nighttime continuous AOD measurements are necessary. In particular, in high latitude regions during the winter polar night, aerosol properties cannot be measured using sunlight, and this results in gaps in the long-term aerosol data. Such nocturnal aerosol data would also contribute to the understanding of aerosol transport to polar regions, the influence of aerosol on cloud formation, and the cloud effect on the radiation budget.

Lidar instruments can be used to obtain aerosol data during the night. However, in many cases, lidar data retrieval requires some physical or mathematical constraints in inversion algorithms to allow the quantitative interpretation of the lidar backscatter signal (Fernald 1984; Klett 1985). In order to improve the accuracy of the analysis, constraining of the AOD is necessary.

In order to measure the optical depth of aerosol at night, research has been conducted using the moon and stars as light sources (Herber et al. 2002; Esposito et al. 1998; Esposito et al. 2003; Pérez-Ramírez et al. 2008). Since the reflectivity of the

moon changes depending on the observation angle, the determination of the calibration coefficient is an important obstacle to overcome (Herber et al. 2002). Instruments for observing stars are large, expensive, and complicated to use due to the low level of incoming energy from stars. Therefore, stellar measurements are limited in use, and no large-scale observation network has been established.

The moon is a bright light source at night and the reflectance properties of the moon's surface are virtually invariant ($<10^{-8}$ yr^{-1}; Kieffer 1997). However, since the surface of the moon is not spatially uniform and has non-Lambertian reflectance, the brightness of the moon as seen by an observer on the earth varies depending on the relationship between the moon, the sun, and the observer, that is, the phase and the lunar libration. Therefore, it is difficult to use the moon as a light source.

However, starting from the 2000s, the quality of reflectance data for the moon has improved. The empirical model known as ROLO (Robotic Lunar Observatory) was developed by the United States Geological Survey (USGS) (Kieffer and Stone 2005). ROLO is a NASA-funded program aimed at using the moon for on-orbit calibration of Earth Observing System (EOS) satellite instruments. Furthermore, the Spectral Profiler (SP) onboard the Japanese Selenological and Engineering Explorer (SELENE, nicknamed Kaguya) measures lunar photometric properties in the region of visible, near-infrared, and shortwave infrared wavelengths (Yokota et al. 2011). These data made it possible to estimate the reflectance of the moon, and thus the moon can be used as a light source for aerosol optical depth estimation.

The Cimel sun photometer used in AERONET has been modified for lunar observation and the aerosol optical depth at night can be estimated (Berkoff et al. 2011; Barreto et al. 2013, 2016, 2017). In addition, a lunar photometer—the Moon Precision Filter Radiometer, LunarPFR (Kouremeti et al. 2016)—has been developed by the Physical Meteorological Observatory in Davos (PMOD), which serves as the World Radiation Center (WRC), based on the sun-PFR experience. Using these instruments and stellar photometers, a multi-instrument nocturnal intercomparison campaign was conducted to evaluate nighttime aerosol measurements and lunar irradiance models (Barreto et al. 2019).

In SKYNET, the radiometers POM-01 and POM-02, manufactured by Prede Co. Ltd., Japan, are used. These radiometers are called 'sky radiometers', and measure both the solar direct irradiance and sky-radiances (Takamura et al. 2004). The sky radiometers POM-01 and POM-02 can measure solar direct irradiance and sky-radiances during the daytime and the measured data are used for estimating aerosol characteristics during the daytime (Takamura et al. 2004). In this study, we will aim to measure the optical depth of aerosol using the moon as a light source by

modifying POM-02.

In section 2, we describe our modification of the instrument. In section 3, the ROLO model is briefly explained. In section 4, we briefly describe the data used in this study. In section 5, the calibration method and corresponding results are described. In section 6, we show the results of comparing the aerosol optical depth and precipitable water vapor obtained by continuous observation with those obtained by other independent instruments. We also show the results of comparing the aerosol optical depth and precipitable water vapor before and after sunrise and sunset using the continuous observation data. Furthermore, we show the results of a comparison between the AERONET and POM-02 data during the period of the MLO calibration measurement.

2. Modification of instrument

In the modification of the POM-02 for solar observation, only the amplifier and the position sensor were changed. The other components, e.g., detectors, filters, and lenses, are not changed. Therefore, the magnitude of the solid view angle (field of view) for the new POM-02 is the same as in the non-modified POM-02. Measurements can still be obtained in the daytime using the modified POM-02.

2.1 Adjustment of Amplifier

The sky radiometer POM-02 is designed to measure the direct solar irradiance and the scattered sky radiance with a single radiometer. An example of the calibration constant, which is the sensor output for the extra-terrestrial solar irradiance at the mean earth-sun distance (1 astronomical unit (AU)) at the reference temperature, is shown in Table 1. The calibration constant is 1.8×10^{-5} to 3.4×10^{-4} A in the visible and near-infrared region, and 7.9×10^{-5} to 1.3×10^{-4} A in the short-wavelength infrared region. Figure 1 shows an example of measurements of scattered radiances in the visible and near-infrared wavelength region. The output for the scattered radiance from the sky is 1×10^{-7} to 1×10^{-10} A, and this value is 1×10^{-6} smaller than the output for the direct solar irradiance. The direct lunar irradiance is 1×10^{-5} as strong as the direct solar irradiance during a full moon, and 1×10^{-6} during a half-moon (Berkoff et al. 2011). From Table 1, the calibration constants at 340 and 380 nm are 1.8×10^{-5} and 1.9×10^{-5} (about 2×10^{-5}), respectively. Therefore, the output for the direct lunar irradiance during the half moon is about $2\times10^{-5} \times 10^{-6} = 2\times10^{-11}$ in the 340 and 380 nm channels. This is close to the detectable limits of the current POM-02. Without

modification, it is possible to measure the direct lunar irradiance with the current POM-02 except for wavelengths between 340 and 380 nm where the sensitivity of the detector is low and wavelengths of 1225, 1627, and 2200 nm with poor S/N.

Table 2 shows the measurement ranges before and after modification of POM-02. POM-02 measures input energy in seven ranges according to the magnitude of the input energy, and the measured value is digitized with 15 bits. After modification the measurement ranges are slightly expanded, and the measurement limit depends on the magnitude of the dark current and the magnitude of the noise. The sensor output takes into account the magnification of the amplifier, and the same amplifier was used for both the solar and lunar measurements.

The dark current of the detector in the visible and near-infrared region was about 5×10^{-13} A, and the RMS of the random component of the noise was 4×10^{-14} A. In consideration of these values, the new POM-02 can use amplifiers for measurement ranges 1 to 7 and the minimum meaningful current is about 4×10^{-13} A (~RMS×10) in the visible and near-infrared region. This value is smaller than the output for the direct solar irradiance by a factor of 1×10^{-8} to 1×10^{-9}.

The dark current of the detector in the shortwave infrared wavelength region was about 1.5×10^{-8} A, and the RMS of the random component of the noise was 4×10^{-11} A. The measurement range is limited due to the large dark current. The new POM-02 can use amplifiers for measurement ranges 1 to 5 and the minimum meaningful current is about 4×10^{-10} A (~RMS×10). This value and the magnitude of the measured value of the direct lunar irradiance are comparable. Therefore, it is difficult to measure the direct lunar irradiance even with the new POM-02 in the shortwave infrared wavelength region.

2.2 Sun and moon position sensor

The tracking of the sun and the moon is based on the calculated position. The moon positions are calculated with the simplified formula in Nagasawa (1981). The necessary software is installed in the firmware of POM-02. Deviations may occur even if the instrument is pointed in the calculated direction due to errors in the moon position calculation, instrument installation errors, misalignment of the rotation axis, and so on. A position sensor is used to correct this deviation.

A position sensor with a four-quadrant detector is used to adjust the tracking of the sun and the moon. In order to adjust the tracking of the moon, a position sensor incorporating a new electronic circuit to amplify the signal and new software to process the signal data were developed. The new position sensor can be used to track

both the sun and the moon.

When the input energy to the position sensor is small, it is difficult to adjust the tracking with the position sensor. The magnitude of the input energy to the position sensor varies depending on the lunar phase and the aerosol optical depth. It was confirmed that the function of the moon tracking adjustment works during the period of the full moon ± about 90 degrees of the phase angle (half-moon).

Whether the position sensor can be used can be determined by a user-specified threshold value. That is, the position sensor can be deactivated when the input energy to the position sensor becomes less than the threshold value. For phase angles larger than the half-moon, the signal of the position sensor was small, and the position sensor was deactivated.

When the position sensor is not functioning, tracking is performed based on the calculated values. When comparing the moon position calculated by this simplified formula with that calculated using the NASA SPICE toolkit (Acton 1996), the difference in the zenith angle is less than 0.01 degrees, and the difference in the azimuth angle is less than 0.04 degrees. The center of the field of view has a flat region of ±0.5 degrees; the flat region is ±0.25 degrees in the solar disk scan. The apparent diameters of the sun and the moon are about 0.5 degrees. Since the calculation error of the moon position is less than 0.25 degrees, if the misalignment of the rotation axis is negligible and POM-02 is installed correctly, it is possible to track the moon using only the calculated positions. In fact, measurements could be made on the day of a full moon ± 10 days (phase angle about 120 degrees). Figure 2 shows an example of the measurements on Oct. 14, 2017 at NOAA/MLO. In this example, the phase angle of the moon is from 117.6 to 118.0 degrees.

3. Robotic Lunar Observatory (ROLO) irradiance model

In order to estimate the aerosol optical thickness using the moon as a light source, measurement of the extra-terrestrial irradiance of the moon is necessary. In this study, a model known as the ROLO irradiance model (Kieffer and Stone 2005) was used. This model was developed at the U.S. Geological Survey (USGS) and is based on an extensive database of radiance images acquired by the ground-based ROLO over more than 8 years. ROLO is a NASA-funded program designed to use the moon for on-orbit calibration of Earth Observing System (EOS) satellite instruments. The empirical irradiance model was developed for 32 wavelengths from 350 to 2450 nm and has the same form for each wavelength. The average residual is less than 1%. The coefficients of the empirical formula were constrained and determined using

data with a phase angle between 1.55 and 97 degrees. The empirically derived analytic form based on the primary geometric variables is as follows:

$$\ln A_k = \sum_{i=0}^{3} a_{ik} g^i + \sum_{j=1}^{3} b_{jk} \Phi^{2j-1} + c_1\phi + c_2\theta + c_3\Phi\phi + c_4\Phi\theta + d_{1k} e^{-g/p_1} + d_{2k} e^{-g/p_2} + d_{3k} \cos((g - p_3)/p_4) \quad (1)$$

where A_k is the disk-equivalent reflectance, g is the absolute phase angle in radians, θ and ϕ are the selenographic latitude and longitude of the observer in degrees, and Φ is the selenographic longitude of the sun in radians.

This formula must be used with caution. The equation in Kieffer and Stone (2005) has well-known typographical errors. In eq. (1), θ and ϕ in the original expression by Kieffer and Stone (2005) are exchanged. In addition, the units of the coefficients p_1, p_2, p_3, and p_4 are degrees. Therefore, in order to make the dimensions the same, g in the exponent and the cosine terms must be converted into units of degrees.

The astronomical parameter was calculated using our own software developed using the NASA SPICE toolkit; an observation geometry information system named SPICE is offered by NASA's Navigation and Ancillary Information Facility (NAIF) (Acton, 1996). SPICE is widely used in the NASA and international planetary exploration communities (for more information about SPICE, refer to the NAIF webpage at http://naif.jpl.nasa.gov.).

In this study, only the values of the reflectance are used, and it is assumed that there is an error in the ROLO reflectance and that the correct reflectance is proportional to the ROLO reflectance. This indicates that the relative variation in the ROLO reflectance is assumed to be correct. The reflectance values are not converted to irradiance values by assuming the extra-terrestrial solar spectral irradiance. The wavelength of POM-02 used in this study does not necessarily match the wavelength of the ROLO model. Here, the reflectance at the wavelength of POM-02 was calculated by linearly interpolating from the reflectance of the ROLO model at two adjacent wavelengths. Information on the filters used in the ROLO measurement was not available. Here, the wavelength is represented by the center wavelength. In addition, the ROLO model does not have reflectance data for the wavelength 340 nm. The reflectance at the wavelength 340 nm was obtained by extrapolating linearly from the values at the two end wavelengths.

4. Data

4.1 Data for Langley calibration

The aerosol optical thickness is estimated by measuring the attenuation of the direct solar or lunar irradiance. Therefore, in order to estimate the aerosol optical thickness, the output of the instrument for the input irradiance at the top of the atmosphere is necessary. The determination of this constant is referred to as calibration, and the output of the instrument for the extra-terrestrial solar or lunar irradiance at the mean earth-sun distance (1 AU) at the reference temperature is called the calibration constant. In this study, the calibration constant was determined by the Langley method.

To calibrate the POM-02 by the Langley method, measurements were conducted at the NOAA Mauna Loa Observatory (MLO) during the period from Sep. 28, 2017 to Nov. 7, 2017; the full moon was on Oct. 4 and Nov. 3, 2017. The MLO (19.5362°N, 155.5763°W) is located at an elevation of 3397.0 meters amsl on the northern slope of Mauna Loa, Island of Hawaii, Hawaii, USA. The atmospheric pressure is about 680 hPa. The MLO is one of the most suitable places to obtain data for a Langley plot for the solar direct irradiance measurement (Shaw 1983). Though the air at MLO is highly transparent, it is affected in the late morning and afternoon hours by marine aerosol that reaches the observatory during the marine inversion boundary layer breakdown under solar heating (Shaw 1983; Perry et al. 1999). Therefore, using data taken in the morning is recommended (Shaw 1982; Dutton et al. 1994; Holben et al. 1998).

However, during the nighttime, the upslope winds change to downslope winds, which bring low moisture and aerosol-poor air above the marine boundary layer down to the observatory. As a result, daytime orographic clouds at the observatory disappear and the atmosphere stratification becomes stable. These atmospheric conditions are suitable for obtaining data for the Langley plot from the lunar direct irradiance measurement.

During the calibration period, the data obtained for the moon over 18 nights for the visible and near-infrared region, and 13 nights for the short wavelength infrared region and water vapor channel (940 nm) were used to determine the calibration constants. The data obtained for the sun over 22 days for the visible, near-infrared, and short wavelength infrared region, and 24 days for the water vapor channel (940 nm) were used to determine the calibration constants.

4.2 Continuous measurement for comparison

The measurements for the estimation of the aerosol optical depth and precipitable

water vapor were performed at 1-minute intervals at the Japan Meteorological Agency/Meteorological Research Institute (JMA/MRI) (36.05°N, 140.13°E) in Tsukuba, which is located about 50 km northeast of Tokyo. The comparison was made using data obtained during the period from Jan. 1 to May 31, 2018. During this period, the AOD and the precipitable water vapor (PWV) were estimated assuming the calibration constant was unchanged.

The optical depth estimated from POM-02 was compared with the value of the National Institute for Environmental Studies (NIES) High Spectral Resolution Lidar (HSRL, wavelength; 532 nm). The NIES/HSRL is one of the lidar operated by the lidar measurement group of the NIES (Shimizu et al. 2016). The NIES and MRI observation sites are located about 800 m apart. Since the POM-02 was not measured at the 532 nm wavelength, the AOD at 532 nm was interpolated from the values of 500 nm and 675 nm by assuming that AOD is proportional to $\lambda^{-\alpha}$, where λ is the wavelength. Furthermore, since the AOD of NIES/HSRL is the 15-minute average, the value of POM-02 was also averaged over 15 minutes.

The PWV estimated from POM-02 was compared with that obtained from the vertical profile of a radiosonde and that obtained from the Global Positioning System (GPS) receiver. The radiosonde observation is operated from the JMA Aerological Observatory, which is adjacent to JMA/MRI. The GPS receiver is installed at JMA/MRI, and GPS data were processed by one of the JMA/MRI researchers (Shoji et al. 2013). The comparison of the PWV was performed using the 30-minute average values.

5. Calibration of POM-02 using MLO data

5.1 Langley method

In this study, the calibration constant was determined by the Langley method (Uchiyama et al. 2018). Here, we do not consider the temperature dependence of the sensor output for the POM-02. Under these observation conditions in Tsukuba, the temperature dependence of the sensor output can be ignored except for the 340, 380, and 2200 nm channels (Uchiyama et al. 2018).

The sensor output when measuring the direct solar irradiance can be written as follows:

$$V(\lambda_0) = \frac{V_{S0}(\lambda_0)}{{R_S}^2} \exp(-m(\theta)\tau(\lambda_0))\bar{T}_{gas}(\lambda_0, \theta) \quad (2)$$

where $V(\lambda_0)$ is the sensor output in the λ_0 wavelength channel, R_S is the earth-sun distance in AU, $m(\theta)$ is the total airmass, $\tau(\lambda)$ is the total optical

depth, θ is the solar zenith angle, and $\bar{T}_{gas}(\lambda_0,\theta)$ is the channel average transmittance of the gas line absorption. Furthermore, $V_{S0}(\lambda_0)$ is the sensor output for the extra-terrestrial solar irradiance at 1 AU, and is called the calibration constant. $\tau(\lambda)$ consists of the optical thickness for molecular scattering (Rayleigh scattering), aerosol, and the continuous absorption of gas. In this study, it is assumed that airmass $m(\theta)$ is the same for all components. The airmass $m(\theta)$ for molecular scattering is used (Schmid and Wehrli 1995; Holben et al. 1998).

In the case of no "gas absorption", the following equation is used:

$$V(\lambda_0) = \frac{V_{S0}(\lambda_0)}{R_S{}^2} \exp(-m(\theta)\tau(\lambda_0)) \tag{3}$$

Taking the logarithm of the equation leads to

$$\begin{aligned} \ln(V(\lambda_0)R_S{}^2) &= \ln V_{S0}(\lambda_0) - m(\theta)\tau(\lambda_0) \\ &= C_1 m(\theta) + C_2 \end{aligned} \tag{4}$$

The parameters on the left-hand side are known: V is the measurement value, and R_S and $m(\theta)$ can be calculated from the solar zenith angle. For example, R_S can be calculated with the simplified formula in Nagasawa (1981), and $m(\theta)$ can be calculated as in Kasten and Young (1989). In the case of POM-02, the sensor output is the current, and the unit of the measurements of V is the ampere A. $C_2 = \ln V_{S0}$ is determined from the ordinate intercept of a least-square fit when one plots the left-hand side of the above equation versus airmass $m(\theta)$.

For the water vapor absorption band at a wavelength of 940 nm, the Beer-Lambert-Bouguer law is not valid. Calibration methods for the 940 nm channel, which is in the water vapor absorption band, have been considered extensively in previous studies (Reagan et al. 1987a, 1987b, 1995; Bruegge et al. 1992; Thome et al. 1992, 1994; Michalsky et al. 1995, 2001; Schmid et al. 1996, 2001; Shiobara et al. 1996; Halthore et al. 1997; Cachorro et al. 1998; Plana-Fattori et al. 1998, 2004; Ingold et al. 2000; Kiedron et al. 2001, 2003; Uchiyama et al. 2014, Campanelli et al. 2014).

In this study, the modified Langley method is used (Reagan et al. 1987a; Bruegge et al. 1992; Schmid and Wehrli 1995). In the modified Langley method, the transmittance is approximated by an empirical formula. The water vapor transmittance is approximated as follows:

$$Tr(\mathrm{H2O}) = \exp(-a(m(\theta)\cdot pwv)^b) \tag{5}$$

where a and b are fitting coefficients, and pwv is PWV.

Coefficients a and b were determined by computing the transmittance for several

atmospheric models (Uchiyama et al. 2014).

The output of the 940 nm channel can be written as follows:

$$V(\lambda_0) = \frac{V_{S0}(\lambda_0)}{R_S^{\,2}} \exp(-m(\theta)\tau(\lambda_0))Tr(\mathrm{H2O}) = \frac{V_{S0}(\lambda_0)}{R_S^{\,2}} \exp(-m(\theta)\tau(\lambda_0)) \exp(-a(m(\theta)\cdot pwv)^b) \quad (6)$$

Taking the logarithm of the equation leads to

$$\ln VR_s^{\,2} + m(\theta)(\tau_{aer} + \tau_R) = \ln V_{S0} - a(pwv)^b m(\theta)^b = C_1' m(\theta)^b + C_2' \quad (7)$$

In the same way as the normal Langley method, the parameters on the left-hand side are known: V is the measurement value, and R and $m(\theta)$ can be calculated from the solar zenith angle. τ_R is also estimated from the surface pressure; for example, τ_R can be calculated as in Asano et al. (1983). In addition, τ_{aer} is the aerosol optical depth at the 940 nm wavelength, which is interpolated from the aerosol optical depth from the values at the 870 and 1020 nm wavelengths.

If pwv is constant, then the right-hand side of the equation is a linear function of $m(\theta)^b$. Therefore, the values on the left-hand side can be fitted by a linear function of $m(\theta)^b$, and the intersection of the y-axis and the fitted line is $\ln V_{S0}$.

5.2 Langley method for the moon

The sensor output when measuring the direct lunar irradiance can be written as follows:

$$V(\lambda_0) = \frac{\tilde{A}_{ROLO}}{\pi} \Omega_M \frac{V_{S0}(\lambda_0)}{R_S^{\,2}} \cdot \frac{1}{R_m^{\,2}} \exp(-m(\theta)\tau(\lambda_0)) \overline{T}_{gas}(\lambda_0, \theta) \quad (8)$$

where Ω_M is the solid angle of the moon, R_S is the distance between the moon and the sun in AU, and R_m is the distance between the moon and the observer normalized by 384,400 km (the mean radius of the moon's orbit around the earth). $\tilde{A}_{ROLO}$ is the smoothed ROLO reflectance adjusted to the laboratory reflectance spectra of the Apollo 16 samples. $\tilde{A}_{ROLO}$ is calculated using the lunar reflectance A_{ROLO} with the ROLO irradiance model by the method shown in Kieffer and Stone

426 (2005) (see Appendix A).

427 Let $\tilde{A}_{ROLO} = F_C A_{ROLO}$, where F_C is a constant for smoothing (see Appendix A).

428 Using this equation, eq. (8) becomes

429 $$V(\lambda_0) = \frac{F_C A_{ROLO}}{\pi} \Omega_M \frac{V_{S0}(\lambda_0)}{R_S{}^2} \cdot \frac{1}{R_m{}^2} \exp(-m(\theta)\tau(\lambda_0)) \bar{T}_{gas}(\lambda_0, \theta) \quad (9)$$

430 It is known that the aerosol optical depth retrieved using the ROLO reflectance
431 contains an error, which is dependent on the phase angle (Barreto et al. 2016, 2017,
432 2019, Juryšek and Prouza 2017). We assume that there is an error in the ROLO
433 reflectance and that the correct lunar reflectance is proportional to the ROLO
434 reflectance. This indicates that the relative variation in the ROLO model reflectance
435 is assumed to be correct. Let the proportional constant be denoted C' , and A_{ROLO}
436 in eq. (9) be replaced with $C' \cdot A_{ROLO}$. Equation (9) then becomes
437

438
$$\begin{aligned} V(\lambda_0) &= \frac{F_C C' A_{ROLO}}{\pi} \Omega_M \frac{V_{S0}(\lambda_0)}{R_S{}^2} \cdot \frac{1}{R_m{}^2} \exp(-m(\theta)\tau(\lambda_0)) \bar{T}_{gas}(\lambda_0, \theta) \\ &= \frac{C A_{ROLO}}{\pi} \Omega_M \frac{V_{S0}(\lambda_0)}{R_S{}^2} \cdot \frac{1}{R_m{}^2} \exp(-m(\theta)\tau(\lambda_0)) \bar{T}_{gas}(\lambda_0, \theta) \end{aligned} \quad (10)$$

439 where $F_C C'$ is substituted with C .

440 In the case of no "gas absorption", taking the logarithm of the equation leads to

441
$$\begin{aligned} \ln\left(\frac{\pi V(\lambda_0)}{A_{ROLO}\Omega_M} R_S{}^2 R_m{}^2\right) &= \ln C V_{S0}(\lambda_0) - m(\theta)\tau(\lambda_0) \\ &= \ln V_{m0}(\lambda_0) - m(\theta)\tau(\lambda_0) \\ &= C_1'' m(\theta) + C_2'' \end{aligned} \quad (11)$$

442 where $V_{m0}(\lambda_0) = C V_{S0}(\lambda_0)$. $C_2'' = \ln V_{m0}$ is determined from the ordinate intercept
443 of a least-square fit when one plots the left-hand side of the above equation versus
444 airmass $m(\theta)$.
445 V_{S0} can be determined by applying the Langley method to data taken during the
446 daytime. If V_{S0} is determined, the coefficient C can be determined by taking the
447 ratio of V_{m0} and V_{S0} . If the coefficient C is 1, the reflectance of the ROLO model
448 will be correct. If the coefficient C is greater than 1 (less than 1), the reflectance in
449 the ROLO model is under-estimated (over-estimated).
450

5.2 Results

Examples of Langley plots in the visible and near-infrared wavelengths are shown in Fig. 3. In these examples, the regression lines can be well determined for any wavelength. $C_2'' = \ln V_{m0}$ is determined from the ordinate intercept of the regression line (see eq. (11)). At the 340 nm wavelength, the regression line tends to deviate from the measured values in the region of airmasses larger than 6. It is presumed that the detector output at the 340 nm wavelength is small and hence may be nonlinear. The output at the time of observation was about 1×10^{-12} A. When using output values less than this, the user needs to treat their results with caution. At the 940 nm wavelength, the modified Langley method was applied. In this example, the regression line provides a good fit.

In Fig. 4, examples of the Langley plot in the shortwave infrared region (1225, 1627, 2200 nm) are shown. The detector output of these channels range from 2×10^{-10} to 5×10^{-10} A, and the root mean square error of the random noise is 4×10^{-11} A. The ratio of noise to detector output is large and it is difficult to use these channels for estimating the aerosol optical depth.

In Fig. 5, the relationship between the coefficient $C(=V_{m0}/V_{S0})$ and the phase angle in the visible and near-infrared wavelength region (from 340 to 1020 nm) is shown. As shown in the previous section, the corrected lunar reflectance is assumed to be proportional to the ROLO reflectance, and the proportional coefficient C is the ratio of the calibration constant for the moon and the sun. That is, the coefficient C indicates the error of the ROLO reflectance, and thus more accurate reflectance can be obtained by multiplying the ROLO reflectance by the coefficient C. As can be seen from this figure, the coefficient C is often greater than 1 and depends on the phase angle. At most wavelengths, the coefficient C is small when the absolute value of the phase angle is small (near the full moon) and increases as the absolute value of the phase angle increases. The range of C is 0.95 to 1.18. The absorption band of water vapor is at the 940 nm wavelength. Water vapor in the atmosphere tends to fluctuate. Therefore, it is difficult to make accurate Langley plots, and the accuracy of both V_{S0} and V_{m0} is poor. Therefore, no clear relationship between C and the phase angle is found, but the coefficient C is about 1.16. The fact that C is larger than 1 means that the reflectance of the ROLO irradiance model is underestimated.

In Fig. 6, the relationship between the coefficient $C(=V_{m0}/V_{S0})$ and the phase angle in the shortwave infrared wavelength region (1225, 1627, 2200 nm) is shown.

In these channels, the error for C is large, but the coefficient C depends on the phase angle as in the visible and near-infrared wavelength region; C is small when the phase angle is near zero and increases as the absolute value of the phase angle increases.

In this study, the phase angle dependence of the coefficient C is approximated by a quadratic equation of the absolute value of the phase angle:

$$C = A_c \cdot g^2 + B_c \quad (12)$$

where g is the phase angle.

That is,

$$V_{m0} = V_{S0} \cdot (A_c \cdot g^2 + B_c) \quad (13)$$

The coefficients A_c and B_c are shown in Table 3. The regression line was plotted in Figs. 5 and 6. By using this approximation, the reflectance of the ROLO model can be estimated to within 1% in most channels. By using this approximation, the data processing to estimate the aerosol optical depth from the measured value becomes straightforward. The coefficients, F_C, for smoothing the ROLO reflectance are also shown in Table 3. The coefficients A_c' and B_c' of the regression equation when using the smoothed ROLO reflectance are also given.

The size of the error in the reflectance in the ROLO irradiance model is dependent on the phase angle. The ROLO reflectance was obtained by dividing the lunar irradiance measured by Kieffer and Stone (2005) by the solar spectral irradiance of the 1985 Wehrli Standard Extraterrestrial Solar Irradiance Spectrum (Wehrli 1985, Neckel and Labs 1981). The solar spectral irradiances are dependent on the solar spectral models. Therefore, the ROLO reflectance includes an error due to the error in the solar spectral irradiance of 1985 Wehrli. Instrument performance, data processing, and so on are also sources of error. In this study, C is approximated as a symmetric quadratic equation of the phase angle, but the phase angle dependence of C is asymmetric (see Figs. 5 and 6). The applicable range of the ROLO reflectance model is a phase angle of about 95 degrees or less. In order to improve the accuracy of the ROLO reflectance model and expand its application range, it is necessary to further accumulate the reflectance data of the moon.

6. Results of comparison

In order to validate the estimations of AOD and PWV, we compared them with the AOD and PWV obtained by independent methods. We investigated whether there is

a difference between daytime and nighttime measurements, and compared the measurements for the daytime and nighttime with measurement data which was recorded independently of POM-02 and has the same accuracy and precision in the daytime and nighttime.

Furthermore, the continuity of the AOD and PWV before and after sunrise and sunset was investigated, and the AOD and PWV of AERONET and POM-02 at MLO were also compared.

6.1 Aerosol optical depth (AOD)

The AOD estimated from POM-02 was compared with the value of the NIES/HSRL (wavelength: 532 nm).

Figures 7 (a) and (b) show the scatter plot of the aerosol optical depth during the daytime and nighttime, respectively. In Fig. 7 (c), the scatter plot during the nighttime is shown together with that during the daytime. Table 4 shows the results of the comparison between NIES/HSRL and POM-02 AOD: the statistics of the difference between the two AODs, the coefficients of the linear regression equation of NIES/HSRL and POM-02 AOD ($\tau_{HSRL} = C_1 \cdot \tau_{POM\,02} + C_2$), the RMSE of the residual, the 95% confidence interval of the coefficients, and the number of observations.

The difference in the slope value of the regression coefficients is 0.1600 (= 1.0477 − 0.8877). The 95% confidence interval of the coefficient is about ±0.04 during both the daytime and the nighttime. It cannot be said that the slopes of the two regression lines are equal based on their 95% confidence intervals. However, the correlation between NIES/HSRL and POM-02 AOD is high, and the differences between them and their RMSEs are similar. Furthermore, as shown in Fig. 7 (c), the scatter diagrams for the daytime and nighttime are almost overlapping, and it seems that the two sets of measurements obtained similar results.

Examples of time series of the AOD from NIES/HSRL and POM-02 are shown in Fig. 8. As can be seen from these figures, the AOD of the daytime and nighttime estimated from POM-02 constitute a continuous series. The AOD from NIES/HSRL and that from POM-02 have qualitatively similar time variations. However, in these limited examples, while there are periods when the values are consistent, there are periods when there are systematic differences.

In the NIES/HSRL data processing, the AOD below an altitude of 500 m is calculated by using the value of the extinction coefficient for an altitude of 500 m. Since the height of the atmospheric boundary layer is typically 1500 to 2000 m, a large amount of aerosols exist at altitudes below 500 m. If the actual distribution

559 deviates from the assumed distribution, the estimated AOD is shifted systematically.
560 In Fig. 8 only limited examples were shown, but in the Supplement, the time series
561 of the AOD at 500 nm at Tsukuba for 5 months is shown in Fig. S1. In addition, the
562 time series of the comparison between the HSRL and POM-02 AOD for 5 months is
563 shown in Fig. S3.
564
565 6.2 Precipitable water vapor (PWV)
566
567 The PWV estimated from POM-02 was compared with that obtained from the
568 vertical profile of the radiosonde and that obtained from the GPS receiver. The PWV
569 estimated from the radiosonde data has a frequency of two values per day, whereas
570 the PWV obtained from GPS is continuous.
571
572 6.2.1 Radiosonde
573
574 The PWV from a radiosonde is often used as a reference for the PWV measurement
575 value. The PWV from the radiosonde and PWV from POM-02 are first compared.
576 Figure 9 shows a scatter plot of the PWV from the radiosonde and from POM-02. The
577 red symbol denotes 00 UTC (09 LST), and the blue symbol is 12 UTC (21 LST). Table
578 5 shows the results of the comparison between the radiosonde and POM-02
579 precipitable water vapor (Table 5 is the same as Table 4 except for radiosonde and
580 POM-02 precipitable water vapor).
581 The ratio of PWV estimated from POM-02 and the radiosonde in both daytime and
582 nighttime is almost constant: the slope of the regression line is 0.80 in the daytime
583 and 0.78 in the nighttime.
584 The empirical formula of the transmittance is expressed as eq. (5). The ratio of the
585 two PWVs is almost constant. In addition, as shown in Fig. 5, the modified Langley
586 plot provides a good fit for the data. From these facts, it seems that the value of the
587 coefficient b in eq. (5) is appropriate but the value of the coefficient a in eq. (5)
588 was inappropriate. It is possible that the filter characteristics of the 940 nm channel
589 have changed from the nominal characteristics due to degradation.
590 Let $pwv = c \cdot pwv'$ and rewrite eq. (5) as follows:

591
$$\begin{aligned} Tr(\mathrm{H2O}) &= \exp(-a(m(\theta)\cdot(c\cdot pwv'))^b) \\ &= \exp(-ac^b(m(\theta)\cdot pwv')^b) \end{aligned} \qquad (14)$$

592 Then the PWV can be corrected by replacing a with ac^b.
593 Figure 10 shows a scatter plot of the PWV from the radiosonde and the corrected

PWV from POM-02. For the correction coefficient c, the average value of the coefficients C_1 of the daytime and nighttime regression equations was used. Table 6 shows the results of the comparison between the radiosonde and corrected POM-02 precipitable water vapor (Table 6 is the same as Table 4 except for radiosonde and corrected POM-02 precipitable water vapor).

The slope C_1 of the regression line during the daytime and nighttime is 1.0160 and 0.9869, respectively, and the difference between them is 0.0291 (= 1.0160 − 0.9869). The 95% confidence intervals of the slopes during the daytime and nighttime are ±0.0206 and ±0.0271, respectively. The difference between them is 0.0291, which is larger than the respective 95% confidence intervals. Therefore, the two slopes are not equivalent based on the 95% confidence intervals.

However, since the slope of the regression line determined using all of the data is 1.0042 and the 95% confidence interval is ±0.0173, the three slopes of the regression lines can be regarded as equivalent at the 95% confidence level. Furthermore, there are no large differences in the bias, RMSE, and correlation coefficient between PWV from the radiosonde and POM-02. Therefore, the PWVs of daytime and nighttime for POM-02 are statistically equivalent. That is, both PWVs are presumed to have the same degree of precision and accuracy within the measurement uncertainty.

6.2.2 GPS

Next, the result of the comparison between the PWV obtained from POM-02 and GPS is shown. Before that, the result of the comparison between the PWV obtained from GPS and the radiosonde is shown in Fig. 11. Table 7 shows the results of the comparison between GPS and radiosonde precipitable water vapor (Table 7 is the same as Table 4 except for GPS and radiosonde precipitable water vapor).

The slope of the regression line in Fig. 11 is about 0.94. In the region of the PWV less than 2 g/cm^2, the PWV from GPS tends to be smaller than the PWV from the radiosonde. In the region of PWV more than 3 g/cm^2, the difference between PWV from GPS and the radiosonde is more scattered. Therefore, the slope of the regression line became smaller than 1. In a previous comparison conducted by the authors, the slope of the regression line was almost 1 (Uchiyama et al. 2014). There is a possibility that the PWV from GPS used in this study has a larger error than the PWV used previously.

Figure 12 shows a scatter diagram of the PWV from GPS and the corrected PWV from POM-02. Table 8 shows the results of the comparison between PWV from GPS and corrected PWV from POM-02 (Table 8 is the same as Table 4 except for GPS and

631 corrected POM-02 precipitable water vapor).
632 The slope of the regression line is about 0.91 for both the daytime and nighttime.
633 Similar to the results of the comparison between the PWV from the radiosonde and
634 GPS, in the region of PWV from GPS less than 2 g/cm^2, the PWV from GPS tends to
635 be somewhat smaller than the PWV from POM-02 during both the daytime and
636 nighttime. In the region of PWV greater than 3 g/cm^2, the difference between the
637 PWV from GPS and the radiosonde is more scattered.
638 The difference between the slopes of the regression lines is 0.0076 (= 0.9132 −
639 0.9056) and the 95% confidence intervals during the daytime and nighttime are
640 ±0.0097 and ±0.0221, respectively. Therefore, the confidence intervals of the two
641 slopes are overlapping, and the values of slopes can be regarded as equivalent at the
642 95% confidence level.
643 In Fig. 12 (c), the scatter plot obtained using nighttime data is shown together
644 with that obtained using daytime data. The data obtained during the daytime and
645 nighttime overlap, and it seems that the PWV from POM-02 during the daytime and
646 nighttime are estimated with the same degree of precision and accuracy.
647 Examples of time series of PWV from GPS and POM-02 are shown in Fig. 13. The
648 PWV from GPS and that from POM-02 have qualitatively similar time variations. In
649 these limited examples, although there are some systematic differences in Fig. 13 (b),
650 the PWV from GPS and the PWV from POM-02 almost overlap in Figs. 13 (a) and (c).
651 In addition, the PWV during the daytime and nighttime estimated from POM-02 are
652 continuously connected.
653 In Fig. 13, only limited examples were shown, but in the Supplement, the time
654 series of the PWV at Tsukuba for 5 months is shown in Fig. S2. In addition, the time
655 series of the comparison between GPS and POM-02 PWV for 5 months is shown in
656 Fig. S4.
657
658 6.3 Comparison of AOD (PVW) before and after sunrise and sunset
659
660 The comparison of the AOD (PWV) before and after sunrise and sunset is used to
661 evaluate the moon photometry (Berkoff et al. 2011, Barreto et al. 2013, 2016, 2017,
662 2019).
663 Before and after sunrise (sunset), the AOD before sunrise (after sunset) is the
664 average of the data with a solar altitude angle between −10 and −15 degrees, with a
665 lunar phase angle less than 100 degrees, and with a lunar altitude angle of more
666 than 10 degrees. The AOD after sunrise (before sunset) is the average of the data
667 with a solar altitude angle between 10 and 15 degrees. Since this comparison is

effective when the atmosphere is stable, only data with small variations were selected; standard deviation / average value is less than 0.1 or standard deviation is less than 0.02.

Figure 14 shows a scatter plot of the AOD at the wavelengths of 340, 380, 400, 500, 675, 870, and 1020 nm, and the PWV from the 940 nm channel. Table 9 shows the results of the comparison between the AOD (PWV) from the sun and from the moon (The contents of Table 9 are the same as Table 4 except for the AOD (PWV) from the sun and the moon).

The biases at wavelengths of 340 and 380 nm are relatively large, 0.05 and 0.03, respectively, but the biases at other wavelengths are 0.007 or less. The bias and RMSE of the PWV are 0.02 and 0.14, respectively, which are comparable to those from the comparison with POM-02 and the radiosonde or GPS. The correlation coefficient is high for all wavelengths; 0.65 at a wavelength of 340 nm, and 0.97 or higher at other wavelengths. Furthermore, the 95% confidence interval of the slope value of the regression line includes 1, and the 95% confidence interval of the intercept value includes 0. That is, the regression line is not different from a straight line with a slope of 1 and zero intercept at the 95% confidence level. From these facts, the AOD and PWV retrieved using the moon as the light source are considered to be the same as those retrieved using the sun as the light source at the 95% confidence level.

6.4 Comparison between AERONET and POM-02

There is an AERONET observation site at MLO. In the nighttime, the AODs at wavelengths of 500, 675, 870, and 1020 nm, and the PWV can be compared. In addition to these channels, the AOD at wavelengths of 340, 380, 1020, and 1627 nm can be compared in the daytime. The AERONET data used here are “level 2.0” in the daytime and “level 1.5” in the nighttime. There were no “level 2.0” nighttime data. AERONET “level 1.5” is cloud-screened data but may not have had the final calibration applied. Thus, these data are not quality assured. AERONET “level 2.0” has pre- and post-field calibration applied, cloud-screened, and quality-assured data (see the AERONET homepage, https://aeronet.gsfc.nasa.gov/). The nighttime comparison in this paper uses the AERONET data without quality assurance.

Figure 15 shows a scatter plot of the AERONET and POM-02 AOD (PWV). The blue (red) symbols show the daytime (nighttime) data. Both the daytime and the nighttime data are overlaid; the AOD at wavelengths of 500, 675, 870, 1020, 1627 nm, and the PWV from the 940 nm channel. The plotted data are the 15-minute averages.

The number of measurements for POM-02 in a 15-minute interval is 10 to 16, and that for AERONET is 1 to 6. Only POM-02 data showing small variations were selected; (standard deviation)/average is less than 0.1 or standard deviation is less than 0.02.

Table 10 shows the results of the comparison between the AERONET and POM-02 aerosol optical depth (precipitable water vapor) (Table 10 is the same as Table 4 except for AERONET and POM-02 aerosol optical depth (precipitable water vapor)). The values at 940 nm are the precipitable water vapor.

In the daytime, from Fig. 15, it can be seen that the differences between AERONET and POM-02 AOD (PWV) are small. The 95% confidence interval for the slope of the regression line does not necessarily include 1, but the slope value is nearly 1: between 0.97 and 1.11. The 95% confidence interval for the intercept of the regression line does not necessarily include 0, but the magnitude of the intercept is 0.01 or less except for the 380 nm channel (0.015). The same can be said for the PWV of the 940 nm channel. In addition, the bias and RMSE are less than 0.01 except for the 380 nm channel (0.015), and those for the PWV at 940 nm are 0.018 and 0.022, respectively. Considering that the accuracy of the calibration constant is 0.5 to 1%, these values seem reasonable. Therefore, it can be inferred that in the daytime, POM-02 can measure the AOD (PWV) with the same level of accuracy as AERONET.

In the nighttime, the atmosphere observed at MLO was pristine, and most of the AOD at 500, 675, 870, and 1020 nm were below 0.02. Considering that the accuracy of the calibration constant is 0.5 to 1%, it is difficult to compare the AOD of AERONET and POM-02. In the nighttime, the slope of the regression line deviates from 1 at several wavelengths, but the bias and the RMSE are less than about 0.01. Therefore, the difference between AERONET and POM-02 is small. The slopes of the regression line for the PWV of 940 nm channel in the daytime and the nighttime are 1.07 and 1.16, respectively. Thus, the daytime and nighttime values differ. In the results of section 6.3, there is almost no difference between the daytime and nighttime values. Therefore, this difference may be due to the lack of quality control in the nighttime data.

7. Summary and conclusion

Aerosol data are often estimated using the solar direct irradiance and the solar scattered radiance. Therefore, the majority of data on aerosol properties are obtained using daytime measurements, and there are few data available on aerosol characteristics at night. In order to estimate the aerosol optical depth (AOD) and the

742 precipitable water vapor (PWV) during the nighttime using the moon as a light
743 source, POM-02 (Prede Ltd., Japan), which is used to estimate aerosol characteristics
744 during the daytime, was modified.
745 The current POM-02 has the ability to measure the direct irradiance from the
746 moon for some channels in the visible and near-infrared wavelength region without
747 requiring modification. Several modifications were made to also be able to measure
748 the AOD during the nighttime and expand the measurement ranges.
749 The amplifier was adjusted so that POM-02 could measure up to about 5×10^{-13} A:
750 allowing the lunar direct irradiance to be measured in the wavelength range of 340
751 to 1020 nm.
752 In order to track the moon based on the calculated value, the simplified formula
753 by Nagasawa (1981) was incorporated into the firmware.
754 A position sensor with a four-quadrant detector is used to adjust the tracking of
755 the sun and the moon. In order to adjust the tracking of the moon, a position sensor
756 incorporating a new electronic circuit to amplify the signal and new software to
757 process the signal data were developed. The new position sensor can be used to track
758 both the sun and the moon.
759 The calibration constant was determined by using the Langley method. The
760 measurements of the solar and lunar direct irradiance were conducted at the
761 NOAA/MLO during the period from Sep. 28 to Nov. 7, 2017. Assuming that the
762 correct lunar reflectance is proportional to the ROLO reflectance, the calibration
763 constant for the lunar direct irradiance was determined by using the Langley method.
764 The calibration by the Langley method was successfully performed.
765 The ratio of the calibration constant for the moon to that for the sun was often
766 greater than 1, where the ratio is a coefficient for correcting the ROLO reflectance
767 and includes a smoothing factor. This ratio shows the error of the ROLO irradiance
768 model. The value of the ratio was 0.95 to 1.18 in the visible and near-infrared
769 wavelength region. This means that the ROLO model often underestimates the
770 reflectance. In addition, this ratio depended on the phase angle: when the phase
771 angle was small (near the full moon), the ratio was small, and as the phase angle
772 became larger, the ratio increased. In this study, this ratio was approximated by the
773 quadratic equation of the phase angle. By using this approximation, the reflectance
774 of the moon can be calculated to within an accuracy of 1% or less.
775 The continuous measurement of POM-02 was conducted at JMA/MRI from
776 January 2018 to May 2018, and the AOD and PWV were estimated. In order to
777 validate the estimates of the AOD and PWV, we compared them with the AOD and
778 PWV obtained by independent methods. The AOD was compared with the AOD (532

779 nm) estimated from NIES/HSRL, and the PWV was compared with the PWV from a
780 radiosonde and GPS. In addition, the continuity of the AOD (PVW) before and after
781 sunrise and sunset at Tsukuba was examined, and the AOD (PWV) of AERONET
782 and that of POM-02 at MLO were compared.
783 Concerning the AOD, there were sometimes systematic differences between
784 NIES/HSRL and POM-02. The cause of the systematic differences seems to be that
785 NIES/HSRL assumes a constant extinction coefficient at altitudes of less than 500 m.
786 The slopes of the linear regression lines during the daytime and nighttime could not
787 be said to be equivalent at the 95% confidence level, but the scatter diagrams of the
788 daytime and nighttime were almost overlapping.
789 Concerning the PWV, the slopes of the linear regression lines during the daytime
790 and nighttime were equivalent at the 95% confidence level in the comparisons
791 between the PWV from POM-02 and the radiosonde and in the comparison between
792 the PWV from POM-02 and GPS. Furthermore, the scatter diagrams of the daytime
793 and the nighttime data were almost overlapping.
794 In addition, the comparison of the AOD (PWV) before and after sunrise and sunset
795 showed that the AOD and PWV retrieved using the moon as the light source are the
796 same as those retrieved using the sun as the light source at the 95% confidence level.
797 The comparison of the AOD (PWV) between AERONET and POM-02 was
798 performed using the data taken during the calibration measurements. The
799 comparison in the daytime showed that POM-02 can measure AOD (PWV) with the
800 same accuracy as AERONET. The comparison in the nighttime showed that the
801 difference in the AOD between AERONET and POM-02 was small. However, since
802 there were a lot of optically thin data and AERONET data are not quality-assured,
803 we cannot make a definite conclusion.
804 From these facts, the daytime and nighttime AOD (PWV) measurements are
805 statistically almost equivalent. The AODs (PWVs) during the daytime and nighttime
806 for POM-02 are presumed to have the same degree of precision and accuracy within
807 the measurement uncertainty.
808 The accuracy of the nighttime calibration constant is lower than that for the
809 daytime. The measurement S/N in the nighttime is also worse than that in daytime.
810 Considering these facts, even if there is no statistically significant difference, the
811 magnitude of the error in the AOD (PWV) during the nighttime is not always the
812 same as during the daytime.
813 In this study, the calibration was performed using about 40 days of data including
814 two full moon days. As a result, it was found that there was an error in the
815 reflectance of the ROLO irradiance model. In the future, it is necessary to

accumulate more data for calibration and to reduce the error of the ROLO irradiance model. It is said that the ROLO model can be applied over a phase angle range of about 90 degrees. POM-02 has the ability to measure the direct lunar irradiance up to a phase angle range of about 120 degrees. It is necessary to expand the ROLO irradiance model so that it can be applied to larger phase angles.

It is now possible to estimate the aerosol optical depth during the nighttime. It is necessary to promote the adoption of this system in the existing observation network. After that, the data obtained by using this instrument can be used to better understand nighttime aerosol behavior, for the validation of aerosol transport models, and as input data in assimilation systems.

Appendix A.

The smoothed ROLO reflectance $\tilde{A}_{ROLO}$ can be obtained by the procedure described in Kieffer and Stone (2005).

The calculated reflectance $A_{ROLO}(g,\Phi,\theta,\phi)$ at the 32 ROLO wavelengths for a specific geometric configuration $(g = 7\,\mathrm{deg}, \Phi = 7\,\mathrm{deg}, \theta = 0, \phi = 0)$ is fitted to a composite spectrum of the samples obtained by the Apollo 16 mission with a linear equation of wavelength λ.

$$A_{Apollo} = (a + b\lambda) A_{ROLO}(7,7,0,0) \qquad \text{(a1)}$$

where A_{Apollo} is the composite laboratory reflectance spectrum for the Apollo samples of soil (95%) (Apollo 16 sample 62231, (Pieters 1999)) and breccia (5%) (Apollo 16 sample 67455 (Pieters and Mustard 1988)).

The Apollo sample 62231 spectrum is available at http://www.planetary.brown.edu/pds/AP62231.html. The Apollo sample 67455 spectrum is shown in Fig. 8 in the paper of Pieters and Mustard (1988).

The values of the coefficients a and b are not shown in Kieffer and Stone (2005), but were determined here with the least squares method as follows:

a = 1.640875

b = –1.192034×10^{-4}

where the unit of the wavelengths is nanometers.

By dividing A_{Apollo} by $a+b\lambda$, the smoothed ROLO reflectance for a specific geometric configuration $\tilde{A}_{ROLO}(7,7,0,0)$ can be obtained.

$$\tilde{A}_{ROLO}(7,7,0,0) = A_{Apollo} / (a + b\lambda) \quad \text{(a2)}$$

The smoothed ROLO reflectance $\tilde{A}_{ROLO}(g,\Phi,\theta,\phi)$ for any viewing geometry is given by the following equation:

$$\begin{aligned} \tilde{A}_{ROLO} &= \frac{\tilde{A}_{ROLO}(7,7,0,0)}{A_{ROLO}(7,7,0,0)} A_{ROLO}(g,\Phi,\theta,\phi) \\ &= F_C A_{ROLO}(g,\Phi,\theta,\phi) \end{aligned} \quad \text{(a3)}$$

where $F_C = \tilde{A}_{ROLO}(7,7,0,0) / A_{ROLO}(7,7,0,0)$.

The values of F_C are dependent on the interpolation method of the reflectance table and the accuracy of the values read from the figure. The smoothed and adjusted spectrum $\tilde{A}_{ROLO}(7,7,0,0)$ is shown in Fig. A1. The values of F_C determined by the authors are shown in Table A1 and Fig. A2.

Data availability.

The data used in this study are available from the corresponding author.

Author contributions.

This study was designed by AU, MS, HK, and TM. The measurements for the sky radiometer were conducted by AU, AK, KI, and YW. The adjustment of the amplifier and the development of the position sensor were performed by MS, HK, KI, KK, and YW. The development of the related software and the data analyses were performed by AU. The manuscript was written by AU, and all authors contributed to editing and revision.

Competing interests.

The authors declare that they have no conflict of interest.

Acknowledgements

This work was supported by the NIES GOSAT-2 project, Japan. This work was also supported by JSPS KAKENHI Grant Number 17K00531. We would like to thank Dr. Y. Jin and Dr. T. Nishizawa of NIES for providing the NIES/HSRL data for the comparison of the aerosol optical depth. We also would like to thank Dr. Y. Shoji of

JMA/MRI for providing the GPS data for the comparison of precipitable water vapor. We thank Dr. B. Holben and his staff for their effort in establishing and maintaining the AERONET Mauna Loa site. We would like to thank Dr. T. Stone and two anonymous reviewers for their useful comments.

References

Acton Jr, C. H.: Ancillary data services of NASA's Navigation and Ancillary Information Facility, *Planet. Space Sci.*, **44**, Issue 1, 65-70, 1996.

Asano, S., Murai, K., and Yamauchi, T.: An improvement of the computation method of the atmospheric turbidity factors, *J. Meteorol. Res.*, **35**, 135-144, 1983 (in Japanese).

Barreto, A., Cuevas, E., Damiri, B., Guirado, C., Berkoff, T., Berjón, A. J., Hernández, Y., Almansa, F., and Gil, M.: A new method for nocturnal aerosol measurements with a lunar photometer prototype, *Atmos. Meas. Tech.*, **6**, 585–598, https://doi.org/10.5194/amt-6-585-2013, 2013.

Barreto, Á., Cuevas, E., Granados-Muñoz, M.-J., Alados- Arboledas, L., Romero, P. M., Gröbner, J., Kouremeti, N., Almansa, A. F., Stone, T., Toledano, C., Román, R., Sorokin, M., Holben, B., Canini, M., and Yela, M.: The new sun-skylunar Cimel CE318-T multiband photometer – a comprehensive performance evaluation, *Atmos. Meas. Tech.*, **9**, 631–654, https://doi.org/10.5194/amt-9-631-2016, 2016.

Barreto, Á., Román, R., Cuevas, E., Berjón, A. J., Almansa, A. F., Toledano, C., González, R., Hernández, Y., Blarel, L., Goloub, P., Guirado, C., and Yela, M.: Assessment of nocturnal aerosol optical depth from lunar photometry at the Izaña high mountain observatory, *Atmos. Meas. Tech.*, **10**, 3007–3019, https://doi.org/10.5194/amt-10-3007-2017, 2017.

Barreto, A., Román, R., Cuevas, E., Pérez-Ramírez, D., Berjón, A.J., Kouremeti, N., Kazadzis, S., Gröbner, J., Mazzola, M., Toledano, C., Benavent-Oltra, J.A., Doppler, L., Juryšek, J., Almansa, A.F., Victori, S., Maupin, F., Guirado-Fuentes, C., González, R., Vitale, V., Goloub, P., Blarel, L., Alados-Arboledas, L., Woolliams, E., Taylor, S., Antuña, J.C., Yela, M.: Evaluation of night-time aerosols measurements and lunar irradiance models in the frame of the first multi-instrument nocturnal intercomparison campaign, *Atmospheric Environment* **202**, 190–211, https://doi.org/10.1016/j.atmosenv.2019.01.006, 2019.

Berkoff, T. A., Sorokin, M., Stone, T., Eck, T. F., Hoff, R., Welton, E., and Holben, B.: Nocturnal aerosol optical depth measurements with a small-aperture automated photometer using the moon as a light source, *J. Atmos. Ocean. Tech.*, 28, 1297–1306, https://doi.org/10.1175/JTECH-D-10-05036.1, 2011.

916 Bruegge, C. J., Conel, J. E., Green, R. O., Margolis, J. S., Holm, R. G., and Toon, G.:
917 Water vapor column abundance retrievals during FIFE, *J. Geophys. Res.*, **97**,
918 18,759–18,768, 1992.
919 Cachorro, V. E., Utrillas, P., Vergaz, R., Duran, P., de Frutos, A. M., and
920 Martinez-Lozano, J. A.: Determination of the atmospheric-water-vapor content in
921 the 940-nm absorption band by use of moderate spectral-resolution measurements
922 of direct solar irradiance. *Appl. Opt.*, **37**, 4678–4689, 1998.
923 Campanelli, M., Nakajima, T., Khatri, P., Takamura, T., Uchiyama, A., Estellés, V.,
924 Liberti, G. L., Malvestuto, V.: Retrieval of characteristic parameters for water
925 vapour transmittance in the development of ground based Sun-Sky radiometric
926 measurements of columnar water vapour, *Atmos. Meas. Tech.*, **7**, 1075–1087,
927 doi:10.5194/amt-7-1075-2014, 2014.
928 Dockery, D. W., Pope, C. A., Xu, X., Spengler, J. D., Ware, J. H., Fay, M. E., Ferris, Jr.,
929 B. G., and Speizer, F. E.: An Association between Air Pollution and Mortality in Six
930 U.S. Cities. *New Engl. J. Med.*, **329**, 1753-1759, 1993.
931 Dutton, E.G., Reddy, P., Ryan, S., and DeLuisi, J.: Features and Effects of Aerosol
932 Optical Depth Observed at Mauna Loa, Hawaii: 1982-1992. *J. Geophys. Res.* **99**,
933 8295-8306, 1994.
934 Esposito, F., Serio, C., Pavese, G., Auriemma, G., and Satriano, C.: Measurements of
935 nighttime atmospheric optical depth preliminary data from a mountain site in
936 southern Italy. *J. Aerosol Sci.*, 29 (10), 1213–1218, 1998.
937 Esposito, F., Mari, S., Pavese, G., and Serio, C.: Diurnal and Nocturnal
938 Measurements of Aerosol Optical Depth at a Desert Site in Namibia, *Aerosol*
939 *Science and Technology*, **37**, 392-400, DOI: 10.1080/02786820300972, 2003.
940 Fernald, F.G.: Analysis of atmospheric lidar observations: some comments. *Appl. Opt.*
941 **5**, 652–653, https://doi.org/10.1364/AO.23.000652, 1984.
942 Guerrero-Rascado, J. L., Landulfo, E., Antuña, J. C., Barbosa, H. de M. J., Barja, B.,
943 Bastidas, Á. E., Bedoya, A. E., da Costa, R. F., Estevan, R., Forno, R., Gouveia, D.
944 A., Jiménez, C., Larroza E. G., da Silva Lopes, F. J., Montilla-Rosero, E., Moreira,
945 G. de A., Nakaema, W. M., Nisperuza, D., Alegria, D., Múnera, M., Otero, L.,
946 Papandrea, S., Pallota, J. V., Pawelko, E. Quel, E. J., Ristori, P., Rodrigues, P. F.,
947 Salvador, J., Sánchez, M. F., and Silva, A.: Latin American Lidar Network
948 (LALINET) for aerosol research: diagnosis on network instrumentation, *J. Atmos.*
949 *Sol. Terr. Phys.*, **138–139**, 112–120, 2016.
950 Halthore, R. N., Eck, T. F., Holben, B. N., and Markham, B. L.: Sun photometric
951 measurements of atmospheric water vapor column abundance in the 940-nm band.
952 *J. Geophys. Res.*, **102**(D4), 4343–4352, doi:10.1029/96JD03247, 1997.

Herber, A., Thomason, L. W., Gernandt, H., Leiterer, U., Nagel, D., Schulz, K-H., Kaptur, J., Albrecht, T., and Notholt, J.: Continuous day and night aerosol optical depth observations in the Arctic between 1991 and 1999. *J. Geophys. Res.*, 107, 4097, doi:10.1029/2001JD000536, 2002.

Holben, B. N., Eck, T. F., Slutsker, I., Tanré, D., Buis, J. P., Setzer, A., Vermote, E., Reagan, J. A., Kaufman, Y. J., Nakajima, T., Lavenu, F., Jankowiak, I., and Smirnov, A.: AERONET-A federated instrument network and data archive for aerosol characterization. *Remote Sens. Environ.*,**66**, 1-16, 1998.

Ingold, T., Schmid, B., Matzler, C., Demoulin, P., and Kampfer, N.: Modeled and empirical approaches for retrieving columnar water vapor from solar transmittance measurements in the 0.72, 0.82, and 0.94 μm absorption bands. *J. Geophys. Res.*, **105**, 24,327–24,343, 2000.

Juryšek, J., Prouza, M.: Sun/Moon photometer for the Cherenkov Telescope Array - first results, Proceedings of Science, 35th International Cosmic Ray Conference -ICRC2017, 2017.

Kahn, R. A., Gaitley, B. J., Martonchik, J. V., Diner, D. J., Crean, K. A., and Holben, B.: Multiangle Imaging Spectroradiometer (MISR) global aerosol optical depth validation based on 2 years of coincident Aerosol Robotic Network (AERONET) observations. J. Geophys. Res., 110, D10S04, doi:10.1029/2004JD004706, 2005.

Kasten, F., and Young, A. T.: Revised optical air mass tables and approximation formula. *Appl. Opt.,* **28**, 4735–4738, 1989.

Klett, J.D.: Lidar inversion with variable backscatter/extinction ratios. *Appl. Opt.* **11**, 1638–1643, https://doi.org/10.1364/AO.24.001638, 1985.

Kiedron, P., Michalsky, J., Schmid, B., Slater, D., Berndt, J., Harrison, L., Racette, P., Westwater, E., and Han, Y.: A robust retrieval of water vapor column in dry Arctic conditions using the rotating shadowband spectroradiometer. *J. Geophys. Res.*, **106**, 24,007– 24,016, 2001.

Kiedron, P., Berndt, J., Michalsky, J., and Harrison, L.: Column water vapor from diffuse irradiance. *Geophys. Res. Lett.*, **30**(11), 1565, doi:10.1029/2003GL016874, 2003.

Kieffer, H. H.: Photometric stability of the lunar surface. *Icarus*, **130**, 323–327, 1997.

Kieffer, H. H., and Stone, T. C.: The spectral irradiance of the moon. *Astron. J.*, **129**, 2887–2901, 2005.

Kikuchi, M., Murakami, H., Suzuki, K., Nagao, T. M., Higurashi, A.: Improved Hourly Estimates of Aerosol Optical Thickness Using Spatiotemporal Variability Derived From Himawari-8 Geostationary Satellite, *IEEE Trans, Geosci. Remote Sens.*, **56** (6), 3442-3455, doi: 10.1109/TGRS.2018.2800060, 2018.

990 Kouremeti, N., Gröbner, J., Kazadzis, S., Pfiffner, D., Soder, R.: Development of a
991 Lunar PFR. pp. 21.
992 https://www.pmodwrc.ch/wp-content/uploads/2017/09/2015_Annual_Report.pdf,
993 2016.
994 Levis, J. R., Campbell, J. R., Welton, E. J., Stewart, S. A., and Phillip C. Haftings, P.
995 C.: Overview of MPLNET version 3 cloud detection, *J. Atmos. Oceanic Technol.*,
996 **33**, 2113–2134, http://dx.doi.org/10.1175/JTECH-D-15-0190.1, 2016.
997 Lohmann, U., and Feichter, J.: Global indirect aerosol effects: a review. *Atmos. Chem.*
998 *Phys.*, **5**, 715-737, 2005.
999 Michalsky, J. J., Liljegren, J. C., and Harrison, L. C.: A comparison of sun photometer
1000 derivations of total column water vapor and ozone to standard measures of same at
1001 the Southern Great Plains atmospheric radiation measurement site. *J. Geophys.*
1002 *Res.*, **100**, 25,995–26,003, 1995.
1003 Michalsky, J. J., Min, Q., Kiedron, P. W., Slater, D. W., and Barnard, J. C.: A
1004 differential technique to retrieve column water vapor using sun radiometry. *J.*
1005 *Geophys. Res.*, **106**, 17,433–17,442, 2001.
1006 Neckel, H. and Labs, D.: Improved Data of Solar Spectral Irradiance from 0.33 to
1007 1.25 μm, *Sol. Phy.*, **74**, 231-249, doi:10.1007/BF00151293, 1981.
1008 Nagasawa, K.: Tentai no ichi keisan (Position calculation of celestial bodies), Chjin
1009 Shokan, p. 239, 1981 (in Japanese).
1010 Pappalardo, G., Amodeo, A., Apituley, A., Comeron, A., Freudenthaler, V., Linné, H.,
1011 Ansmann, A., Bösenberg, J., D'Amico, G., Mattis, I., Mona, L., Wandinger, U.,
1012 Amiridis, V., Alados-Arboledas, L., Nicolae, D., and Wiegner, M.: EARLINET:
1013 towards an advanced sustainable European aerosol lidar network, *Atmos. Meas.*
1014 *Tech.*, **7**, 2389-2409, https://doi.org/10.5194/amt-7-2389-2014, 2014.
1015 Pérez-Ramírez, D., Aceituno, J., Ruiza, B., Olmo, F. J., and Alados-Arboledas, L.:
1016 Development and calibration of a star photometer to measure the aerosol optical
1017 depth: Smoke observations at a high mountain site. *Atmos. Environ.*, **42**, 2733–
1018 2738, 2008.
1019 Perry K. D., Cahill, T. A., Schnell, R. C., and Harris, J. M.: Long-range transport of
1020 anthropogenic aerosols to the National Oceanic and Atmospheric Administration
1021 baseline station at Mauna Loa Observatory, Hawaii, *J. Geophys. Res.*, **104**, 18,521–
1022 18,533, 1999.
1023 Pieters, C. M.: The Moon as a Calibration Standard Enabled by Lunar Samples, in
1024 New Views of the Moon II: Understanding the Moon through the Integration of
1025 Diverse Datasets, ed. L. Gaddis & C. K. Shearer (Houston: LPI), 47, 1999.
1026 Pieters, C. M., and Mustard, J. F.: Exploration of crustal/mantle material for the

1027 earth and moon using reflectance spectroscopy, Remote Sensing of Environment,
1028 24, 151-178, 1988.
1029 Plana-Fattori, A., Legrand, M., Tanre, D., Devaux, C., Vermeulen, A., and Dubuisson,
1030 P.: Estimating the atmospheric water vapor content from sun photometer
1031 measurements. *J. Appl. Meteorol.*, **37**, 790– 804, 1998.
1032 Plana-Fattori, A., Dubuisson, P., Fomin, B. A., and de Paula Correa, M.: Estimating
1033 the atmospheric water vapor content from multi-filter rotating shadow-band
1034 radiometry at Sao Paulo, Brazil. *Atmos. Res.*, **71**, 171– 192, 2004.
1035 Prados, A. I., Kondragunta, S., Ciren, P., and Knapp, K. R.: GOES Aerosol/Smoke
1036 Product (GASP) over North America: Comparisons to AERONET and MODIS
1037 observations. *J. Geophys. Res.*, **112**, D15201, doi:10.1029/2006JD007968, 2007.
1038 Ramanathan, V., Crutzen, P. J., Kiehl, J. T., and Rosenfeld, D.: Aerosols, Climate,
1039 and the Hydrological Cycle. *Science*, **294**, 2119-2124, 2001.
1040 Reagan, J. A., Thome, K., Herman, B., and Gall, R.: Water vapor measurements in
1041 the 0.94 micron absorption band-Calibration, measurements and data applications.
1042 *in Proc. Int. Geoscience and Remote Sensing '87 Symposium, Ann Arbor, Michigan,*
1043 *IEEE,* pp. 63–67, 1987a.
1044 Reagan, J. A., Pilewskie, P. A., Herman, B. M., and Ben-David, A.: Extrapolation of
1045 Earth-based solar irradiance measurements to exoatmospheric levels for
1046 broad-band and selected absorption-band observations. *IEEE Trans. Geosci.*
1047 *Remote Sens.*, **25**, 647–653, 1987b.
1048 Reagan, J., Thome, K., Herman, B., Stone, R., DeLuisi, J., and Snider, J.: A
1049 comparison of columnar water vapor retrievals obtained with near-IR solar
1050 radiometer and microwave radiometer measurements. *J. Appl. Meteorol.*, **34**,
1051 1384–1391, 1995.
1052 Remer, L. A., Kaufman, Y. J., Tanré, D., Mattoo, S., Chu, D. A., Martins, J. V., Li,
1053 R.-R., Ichoku, C., Levy, R. C., Kleidman, R. G., Eck, T. F., Vermote, E., and Holben,
1054 B. N.: The MODIS aerosol algorithm, products and validation. *J. Atmos. Sci.*, **62**,
1055 947–973, https://doi.org/10.1175/JAS3385.1, 2005.
1056 Schmid, B., and Wehrli, C.: Comparison of Sun photometer calibration by use of the
1057 Langley technique and the standard lamp, *Appl. Opt.*, **34**, 4500–4512, 1995.
1058 Schmid, B., Thome, K. J., Demoulin, P., Peter, R., Matzler, C., and Sekler, J.:
1059 Comparison of modeled and empirical approaches for retrieving columnar water
1060 vapor from solar transmittance measurements in the 0.94-μm region. *J. Geophys.*
1061 *Res.*, **101**, 9345–9358, 1996.
1062 Schmid, B., Michalsky, J. J., Slater, D. W., Barnard, J. C., Halthore, R. N., Liljegren,
1063 J. C., Holben, B. N., Eck, T. F., Livingston, J. M., Russell, P. B., Ingold, T., and

Slutsker, I.: Comparison of columnar water-vapor measurements from solar transmittance methods, *Appl. Opt.*, **40**, 1886–1896, 2001.

Shaw, G. E.: Solar spectral irradiance and atmospheric transmission at Mauna Loa Observatory, *Appl. Opt.*, **21**, 2006–2011, 1982.

Shaw, G. E.: Sun photometry. *Bull. Am. Meteorol. Soc.*, **64**, 4–11, 1983.

Shimizu, A., Nishizawa, T., Jin, Y., Kim, S.-W., Wang, Z., Batdorj, D., Sugimoto, N.: Evolution of a lidar network for tropospheric aerosol detection in East Asia, *Opt. Eng.*, **56**(3), 031219 (2016), doi: 10.1117/1.OE.56.3.031219, 2016.

Shiobara, M., Spinhirne, J. D., Uchiyama, A., and Asano, S.: Optical depth measurements of aerosol, cloud, and water vapor using sun photometers during FIRE Cirrus IFO II. *J. Appl. Meteorol.*, **35**, 36–46, 1996.

Shoji, Y.: Retrieval of Water Vapor Anisotropy using the Japanese Nationwide GPS Array and its Potential for Prediction of Convective Precipitation. *J. Meteor. Soc. Japan*, **91**, 43-62, 2013.

Takamura, T, Nakajima, T., and SKYNET community group: Overview of SKYNET and its Activities. Proceedings of AERONET workshop. *El Arenosillo. Optica Pura y Aplicada,* **37**, 3303–3308, 2004.

Thome, K., Herman, B. M., and Reagan, J. A.: Determination of precipitable water from solar transmission. *J. Appl. Meteorol.*, **31**, 157-165, 1992.

Thome, K. J., Smith, M. W., Palmer, J. M., and Reagan, J. A.: Three-channel solar radiometer for the determination of atmospheric columnar water vapor. *Appl. Opt.*, **33**, 5811 –5819, 1994.

Uchiyama, A., Yamazaki, A., Kudo, R.: Column Water Vapor Retrievals from Sky-radiometer (POM-02) 940nm Data. *J. Meteorol. Soc. Japan*, **92A**, 195-203, DOI:10.2151/jmsj.2014-A13, 2014.

Uchiyama, A., Matsunaga, T., and Yamazaki, A.: The instrument constant of sky radiometers (POM-02) – Part 1: Calibration constant, *Atmos. Meas. Tech.*, **11**, 5363-5388, https://doi.org/10.5194/amt-11-5363-2018, 2018.

Wang, M., Bailey, S., and McClain, C. R.: SeaWiFS provides unique global aerosol optical property data. *Eos, Trans. Amer. Geophys. Union*, **81**, 197–202, 2000.

World Health Organisation: WHO Air quality guidelines for particulate matter, ozone, nitrogen dioxide and sulfur dioxide; Global update 2005; Summary of risk assessment. World Health Organization, Geneva, Switzerland, p. 22, 2006.

World Health Organization Regional Office for Europe: Review of Evidence on Health Aspects of Air Pollution–REVIHAAP Project, Technical Report WHO, Copenhagen, p. 298, 2013.

Wehrli, C.: Extraterrestrial Solar Spectrum, Publication no. 615,

Physikalisch-Meteorologisches Observatorium + World Radiation Center (PMO/WRC) Davos Dorf, Switzerland, July 1985.

Wehrli, C.: GAW–PFR: A network of Aerosol Optical Depth observations with Precision Filter Radiometers. In: WMO/GAW Experts workshop on a global surface based network for long term observations of column aerosol optical properties, Tech. rep., GAW Report No. 162, WMO TD No. 1287, ftp://ftp.wmo.int/Documents/PublicWeb/arep/gaw/gaw162.pdf, 2005.

Welton, E. J., Campbell, J. R., Spinhirne, J. D., and Scott, V. S.: Global monitoring of clouds and aerosols using a network of micro-pulse lidar systems. *Lidar Remote Sensing for Industry and Environmental Monitoring*, U. N. Singh, T. Itabe, and N. Sugimoto, Eds., International Society for Optical Engineering (SPIE Proceedings, Vol. 4153), 151–158, 2001.

Winker, D. M., Hunt, W. H., and McGill, M. J.: Initial performance assessment of CALIOP. Geophys. *Res. Lett.*, **34**, L19803, doi:10.1029/2007GL030135, 2007.

Yokota, Y., Matsunaga, T., Ohtake, M., Haruyama, J., Nakamura, R., Yamamoto, S., Ogawa, Y., Morota, T., Honda, C., Saiki, K., Nagasawa, K., Kitazato, K., Sasaki, S., Iwasaki, A., Demura, H., Hirata, N., Hiroi, T., Honda, R., Iijima, Y., Mizutani, H.: Lunar photometric properties at wavelengths 0.5–1.6 μm acquired by SELENE Spectral Profiler and their dependency on local albedo and latitudinal zones, *Icarus*, **215**, 639-660, 2011.

Yoshida, M., Kikuchi, M., Nagao, T. M., Murakami, H., Nomaki, T., Higurashi, A.: Common Retrieval of Aerosol Properties for Imaging Satellite Sensors, *J. Meteorol. Soc. Jpn.*, **96B**, 193-209, doi: 10.2151/jmsj.2018-039, 2018.

Table 1 Examples of calibration coefficient V_{S0} for the solar measurement.

Table 2 Measurement ranges before (current) and after modification (new) of POM-02. I_n and I_{n-1} are the upper and lower limits of the current (unit: A), respectively.

Table 3 Coefficients of the regression equation for reflectance correction factor C.

Table 4 Results of the comparison between NIES/HSRL and POM-02 aerosol optical depth.

Table 5 Same as Table 4 except for radiosonde and POM-02 precipitable water vapor.

Table 6 Same as Table 4 except for radiosonde and corrected POM-02 precipitable water vapor.

Table 7 Same as Table 4 except for GPS and radiosonde precipitable water vapor.

Table 8 Same as Table 4 except for GPS and corrected POM-02 precipitable water vapor.

Table 9 Same as Table 4 except for the AOD (PWV) from the sun and the moon.

Table 10 Same as Table 4 except for the AERONET and POM-02 aerosol optical depth (precipitable water vapor).

Figure captions

Fig. 1 An example of sensor output for the solar direct irradiances and the scattered sky radiances by POM-02.

Fig. 2 An example of the measurements taken on Oct. 14, 2017 at NOAA/MLO. The phase angle of the moon (right y-axis) is from 117.6 to 118.0 degrees.

Fig. 3 Examples of the Langley plot in the visible and near-infrared region on Nov. 5, 2017. The y-axis is the equation in parentheses on the left-hand side of eq. (11). (a) 340, 380, 400, 500 nm; (b) 675, 870, 1020 nm; (c) 940 nm, modified Langley

method.

Fig. 4 Examples of the Langley plot in the shortwave infrared region.

Fig. 5 Relationship between phase angle and reflectance correction factor $C = V_{m0} / V_{S0}$ in the visible and near-infrared region. A regression curve ($C = A_c \cdot g^2 + B_c$, g: phase angle) was also plotted.

Fig. 6 Relationship between phase angle and reflectance correction factor $C = V_{m0} / V_{S0}$ in the shortwave infrared region. A regression curve ($C = A_c \cdot g^2 + B_c$, g: Phase angle) was also plotted.

Fig. 7 Scatter plot of HSRL and POM-02 aerosol optical depth at 532 nm. (a) daytime (red), (b) nighttime (blue), (c) overlapping daytime (red) with nighttime (blue).

Fig. 8 Examples of time series of HSRL (red), POM-02 daytime (green) and nighttime (blue) aerosol optical depths at 532 nm. The phase angles (g) during the measurement periods were (a) g = −21.863 to 35.881 degrees, (b) g = 47.454 to 83.190 degrees, and (c) g = −19.150 to 21.573 degrees.

Fig. 9 Scatter plot of radiosonde and POM-02 precipitable water vapor. Daytime (nighttime) measurements are indicated by a red (blue) symbol.

Fig. 10 Same as Fig. 9 except for corrected POM-02 precipitable water vapor.

Fig. 11 Scatter plot of GPS and radiosonde precipitable water vapor.

Fig. 12 Scatter plot of PWV from GPS and corrected PWV from POM-02. (a) daytime (red), (b) nighttime (blue), (c) overlapping daytime (red) with nighttime (blue).

Fig. 13 Examples of time series of GPS (red), POM-02 daytime (green) and nighttime (blue) corrected precipitable water vapor. The phase angles (g) during the measurement periods were (a) g = −21.863 to 35.881 degrees, (b) g = −19.150 to 21.573 degrees, and (c) g = -55.145 to 30.611 degrees.

Fig. 14 Scatter plot of the aerosol optical depth (precipitable water vapor) from the sun and the moon. (a) 340 nm AOD, (b) 380 nm AOD, (c) 400 nm AOD, (d) 500 nm

AOD, (e) 675 nm AOD, (f) 870 nm AOD, (g) 940 nm PWV, (h) 1020 nm AOD.

Fig. 15 Scatter plot of AERONET and POM-02 aerosol optical depth (precipitable water vapor). Daytime (nighttime) measurements are indicated by a red (blue) symbol. (a) 340 nm AOD, (b) 380 nm AOD, (c) 500 nm AOD, (d) 675 nm AOD, (e) 870 nm AOD, (f) 940 nm PWV, (g) 1020 nm AOD, (h) 1627 nm AOD.

Appendix A

Table A1 Coefficients for smoothing at the ROLO 32 wavelength.

Fig. A1 Coefficients for smoothing at the ROLO 32 wavelength.

Fig. A2 ROLO smoothed and adjusted reflectance.

Table 1 Examples of calibration coefficient V_{S0} for the solar measurement.

Wavelength (nm)	340	380	400	500	675	870	940	1020
V_{S0} ($\times 10^{-4}$) (A)	0.1799	0.1882	1.603	3.174	3.444	2.299	1.055	1.077

Wavelength (nm)	1225	1627	2200
V_{S0} ($\times 10^{-4}$) (A)	0.9305	1.321	0.7873

Table 2 Measurement range before (current) and after modification (new) of POM-02.
I_n and I_{n-1} are the upper and lower limits of the current (unit: A), respectively.

Range no.		Current			New		
1	$I_1 - I_2$	2.5×10^{-3}	–	2.5×10^{-4}	2.5×10^{-3}	–	1.25×10^{-4}
2	$I_2 - I_3$	2.5×10^{-4}	–	2.5×10^{-5}	1.25×10^{-4}	–	6.25×10^{-6}
3	$I_3 - I_4$	2.5×10^{-5}	–	2.5×10^{-6}	6.25×10^{-6}	–	3.125×10^{-7}
4	$I_4 - I_5$	2.5×10^{-6}	–	2.5×10^{-7}	3.125×10^{-7}	–	1.5625×10^{-8}
5	$I_5 - I_6$	2.5×10^{-7}	–	2.5×10^{-8}	1.5625×10^{-8}	–	7.8125×10^{-10}
6	$I_6 - I_7$	2.5×10^{-8}	–	2.5×10^{-9}	7.8125×10^{-10}	–	3.90625×10^{-11}
7	I_7	2.5×10^{-9}	–	0.0	3.90625×10^{-11}	–	0.0
	I_n	$I_n=I_{n-1}/10$			$I_n=I_{n-1}/20$		

Table 3 Coefficients of the regression equation for reflectance correction factor C.

Wavelength (nm)	A_c	B_c	RMS	F_c	$A_c'=A_c/F_c$	$B_c'=B_c/F_c$	RMS/F_c	No. of data
340	1.3404×10^{-5}	0.98027	0.0152	0.8993	1.4905×10^{-5}	1.09010	0.0169	15
380	1.3512×10^{-5}	1.0674	0.0080	1.0153	1.3309×10^{-5}	1.05140	0.0079	15
400	3.0760×10^{-6}	1.0058	0.0055	0.95270	3.2287×10^{-6}	1.05570	0.0058	15
500	2.2487×10^{-6}	1.1600	0.0058	1.0184	2.2081×10^{-6}	1.13910	0.0057	15
675	4.8644×10^{-6}	1.0840	0.0048	0.95705	5.0827×10^{-6}	1.13260	0.0050	15
870	3.4967×10^{-6}	1.0855	0.0026	0.95705	3.6537×10^{-6}	1.13420	0.0027	15
940	7.2405×10^{-8}	1.1532	0.0404	1.0292	7.0352×10^{-8}	1.12050	0.0392	13
1020	6.7912×10^{-6}	1.0559	0.0078	0.97065	6.9966×10^{-6}	1.08790	0.0081	15
1225	9.0288×10^{-5}	1.0572	0.0328	1.0203	8.8491×10^{-5}	1.03620	0.0322	13
1627	2.3828×10^{-5}	1.0810	0.0237	1.0463	2.2774×10^{-5}	1.03310	0.0227	13
2200	3.7545×10^{-6}	0.95311	0.0386	0.97493	3.8511×10^{-5}	0.97763	0.0396	13

$C = A_c \cdot g^2 + B_c$

g: phase angle (degrees)

F_c: smoothing factor

Table 4 Results of the comparison between NIES/HSRL and POM-02 aerosol optical depth.

POM-02	Bias	RMSE	CR	C_1	C.I. of C_1 (95%)	C_2	C.I. of C_2 (95%)	RMSE of reg.	NO of obs.
Sun+Moon	0.0437	0.0839	0.8266	0.9611	±0.0295	0.0486	±0.0049	0.0715	1889
Sun	0.0432	0.0866	0.7650	0.8877	±0.0425	0.0573	±0.0068	0.0743	1192
Moon	0.0466	0.0838	0.8825	1.0477	±0.0414	0.0405	±0.0074	0.0694	702

RMSE: Root mean square error

CR: Correlation coefficient

C_1 and C_2: coefficients of regression line ($\tau_{HSRL} = C_1 \cdot \tau_{POM-02} + C_2$)

C.I. of C_1 (95%): 95% confidential interval of C_1

C.I. of C_2 (95%): 95% confidential interval of C_2

RMSE of reg.: RMSE of regression line

Table 5 Same as Table 4 except for radiosonde and POM-02 precipitable water vapor.

POM-02	Bias	RMSE	CR	C_1	C.I. of C_1 (95%)	C_2	C.I. of C_2 (95%)	RMSE of reg.	No. of obs.
Sun+Moon	−0.2477	0.3037	0.9946	0.7948	±0.0138	−0.0057	±0.0196	0.0658	141
Sun	−0.2206	0.2764	0.9945	0.8041	±0.0165	−0.0044	±0.0223	0.0661	104
Moon	−0.3259	0.3726	0.9966	0.7811	±0.0214	−0.0212	±0.0343	0.0508	37

PWV, Bias, RMSE, RMSE of reg.: g/cm^2

C_1 and C_2: coefficients of regression line ($PWV_{POM-02} = C_1 \cdot PWV_{Sonde} + C_2$).

Table 6 Same as Table 4 except for radiosonde and corrected POM-02 precipitable water vapor.

POM-02	Bias	RMSE	CR	C_1	C.I. of C_1 (95%)	C_2	C.I. of C_2 (95%)	RMSE of reg.	No. of obs.
Sun+Moon	−0.0027	0.0830	0.9946	1.0042	±0.0173	−0.0077	±0.0246	0.0829	142
Sun	0.0115	0.0848	0.9945	1.0160	±0.0206	−0.0061	±0.0278	0.0831	105
Moon	−0.0454	0.0794	0.9966	0.9869	±0.0271	−0.0272	±0.0434	0.0643	37

C_1 and C_2: coefficients of regression line ($PWV_{POM-02}(corrected) = C_1 \cdot PWV_{Sonde} + C_2$).

Table 7 Same as Table 4 except for GPS and radiosonde precipitable water vapor.

Sonde	Bias	RMSE	CR	C_1	C.I. of C_1 (95%)	C_2	C.I. of C_2 (95%)	RMSE of reg.	No. of obs.
Sonde	0.0770	0.2229	0.9791	0.9425	±0.0233	0.1572	±0.0403	0.2007	274

C_1 and C_2: coefficients of regression line ($PWV_{Sonde} = C_1 \cdot PWV_{GPS} + C_2$).

Table 8 Same as Table 4 except for GPS and corrected POM-02 precipitable water vapor.

POM-02	Bias	RMSE	CR	C_1	C.I. of C_1 (95%)	C_2	C.I. of C_2 (95%)	RMSE of reg.	No. of obs.
Sun+Moon	0.0159	0.2050	0.9664	0.9032	±0.0089	0.1255	±0.0122	0.1896	2826
Sun	0.0072	0.1939	0.9706	0.9056	±0.0097	0.1164	±0.0137	0.1787	2046
Moon	0.0391	0.2232	0.9527	0.9132	±0.0221	0.1292	±0.0279	0.2106	671

C_1 and C_2: coefficients of regression line ($PWV_{POM-02}(corrected) = C_1 \cdot PWV_{GPS} + C_2$).

Table 9 Same as Table 4 except for the AOD (PWV) from the sun and the moon.

Wavelength (nm)	Bias	RMSE	CR	C_1	C.I. of C_1 (95%)	C_2	C.I. of C_2 (95%)	RMSE of reg.	No. of obs.
340	−0.0527	0.0663	0.6485	0.7309	0.8335	−0.0216	0.1034	0.0384	7
380	−0.0289	0.0425	0.9726	0.9278	0.1042	−0.0136	0.0261	0.0296	20
400	−0.0058	0.0369	0.9700	0.9832	0.0874	−0.0016	0.0256	0.0363	33
500	0.0068	0.0295	0.9734	1.0282	0.0905	0.0017	0.0196	0.0285	30
675	0.0039	0.0216	0.9717	1.0387	0.1021	−0.0010	0.0153	0.0210	26
870	0.0020	0.0149	0.9806	1.0485	0.0830	−0.0023	0.0093	0.0144	27
940	−0.0236	0.1376	0.9751	1.0417	0.0730	−0.0670	0.0865	0.1335	43
1020	0.0047	0.0152	0.9735	1.0726	0.1020	−0.0008	0.0095	0.0139	26

C_1 and C_2: coefficients of the regression line ($\tau_{Moon} = C_1 \cdot \tau_{Sun} + C_2$, $PWV_{Moon} = C_1 \cdot PWV_{Sun} + C_2$).

Table 10 Same as Table 4 except for the AERONET and POM-02 aerosol optical depth (precipitable water vapor).

POM-02	Wavelength (nm)	Bias	RMSE	CR	C_1	C. I. of C_1 (95%)	C_2	C. I. of C_2 (95%)	RMSE of reg.	No. of obs.
Sun	340	0.0082	0.0091	0.9855	0.9722	0.0212	0.0086	0.0006	0.0040	242
Moon	340	-----	-----	-----	-----	-----	-----	-----	-----	0
Sun	380	0.0148	0.0153	0.9819	0.9840	0.0237	0.0151	0.0006	0.0037	249
Moon	380	-----	-----	-----	-----	-----	-----	-----	-----	0
Sun	500	−0.0046	0.0050	0.9884	1.0060	0.0196	−0.0046	0.0004	0.0021	243
Moon	500	−0.0010	0.0054	0.7366	0.6369	0.1524	0.0044	0.0025	0.0045	59
Sun	675	0.0083	0.0085	0.9839	1.0279	0.0235	0.0081	0.0003	0.0018	245
Moon	675	0.0109	0.0112	0.8466	0.8119	0.1368	0.0123	0.0012	0.0024	56
Sun	870	−0.0015	0.0020	0.9877	1.0459	0.0210	−0.0018	0.0002	0.0013	241
Moon	870	−0.0044	0.0059	0.7343	0.5275	0.1283	0.0004	0.0015	0.0028	58
Sun	940	0.0177	0.0223	0.9996	1.0712	0.0038	−0.0025	0.0013	0.0054	259
Moon	940	0.0445	0.0535	0.9991	1.1610	0.0126	0.0035	0.0039	0.0086	59
Sun	1020	0.0017	0.0023	0.9796	1.0393	0.0269	0.0015	0.0002	0.0015	244
Moon	1020	−0.0042	0.0080	0.4128	0.2846	0.1652	0.0038	0.0022	0.0045	58
Sun	1627	0.0020	0.0029	0.9828	1.1100	0.0359	0.0017	0.0003	0.0019	132
Moon	1627	-----	-----	-----	-----	-----	-----	-----	-----	0

Table A1 Coefficients for smoothing at the ROLO 32 wavelength

Wavelength (nm)	Correction factor	Wavelength (nm)	Correction factor
350.0	1.02766	763.7	1.00312
355.1	1.09314	774.8	0.95628
405.0	0.93705	865.3	0.94167
412.3	0.95166	872.6	0.96555
414.4	1.02732	882.0	0.94490
441.6	1.01667	928.4	0.97167
465.8	1.04970	939.3	1.04085
475.0	1.01461	942.1	0.99417
486.9	1.01748	1059.5	0.95872
544.0	1.02132	1243.2	1.02708
549.1	0.99098	1538.7	1.02616
553.8	1.02041	1633.6	1.04781
665.1	0.93882	1981.5	1.05865
693.1	0.99039	2126.3	1.08338
703.6	1.00576	2250.9	0.90003
745.3	0.99651	2383.6	0.98073

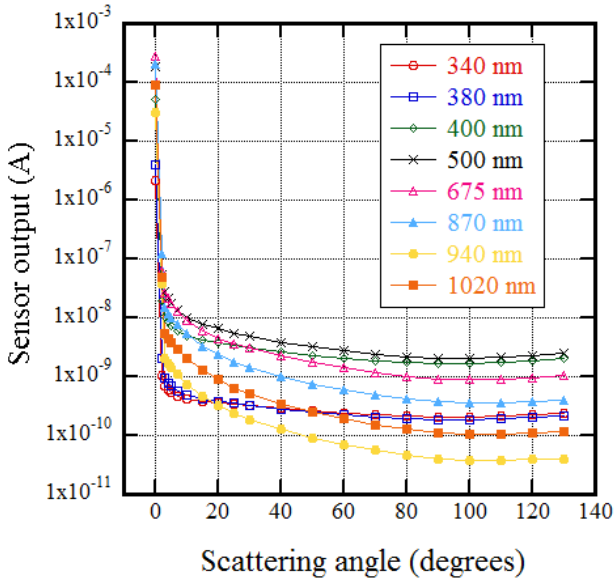

Fig. 1 Examples of sensor output for solar direct irradiances and scattered sky radiances from POM-02.

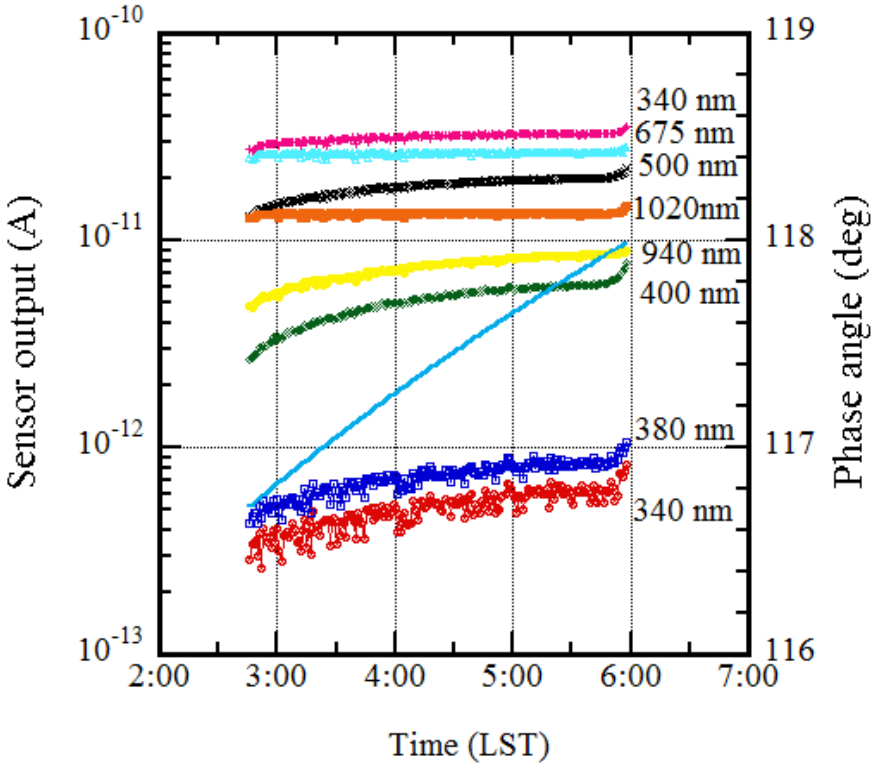

Fig. 2 An example of the measurements taken on Oct. 14, 2017 at NOAA/MLO. The phase angle of the moon (right y-axis) is from 117.6 to 118.0 degrees.

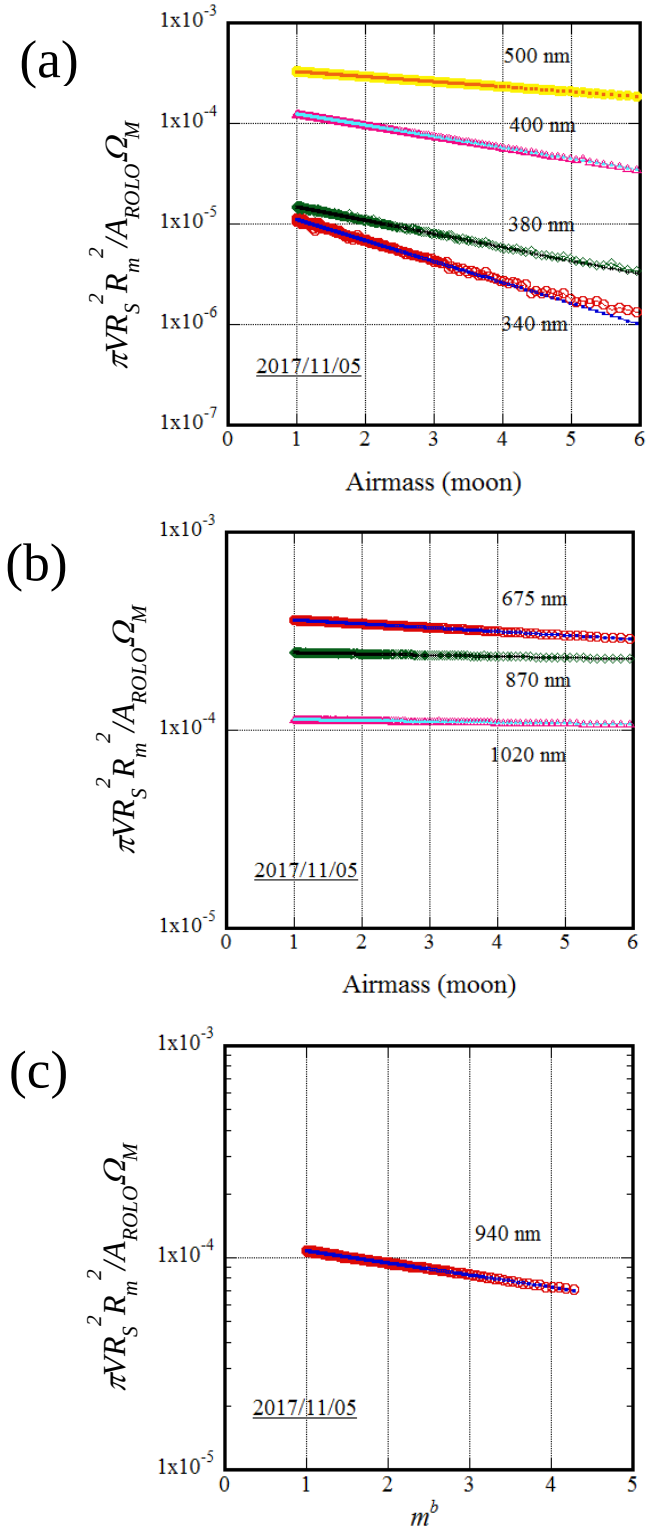

Fig. 3 Examples of the Langley plot in the visible and near-infrared region on Nov. 5, 2017. The y-axis is the equation in parentheses on the left-hand side of eq. (10).
(a) 340, 380, 400, 500 nm; (b) 675, 870, 1020 nm; (c) 940 nm, modified Langley method.

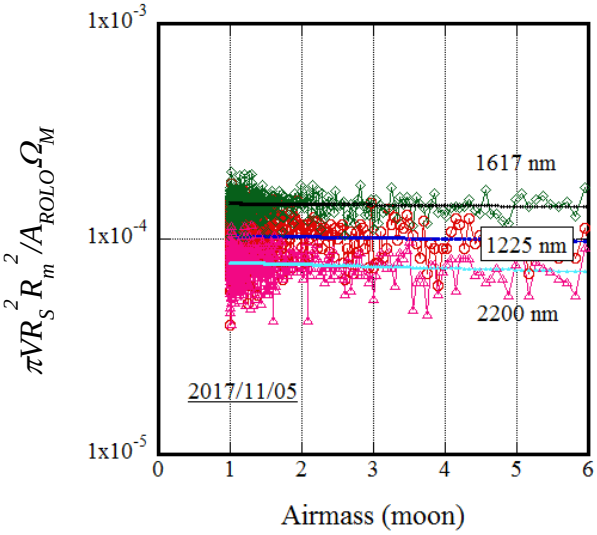

Fig. 4 Examples of the Langley plots in the shortwave infrared region.

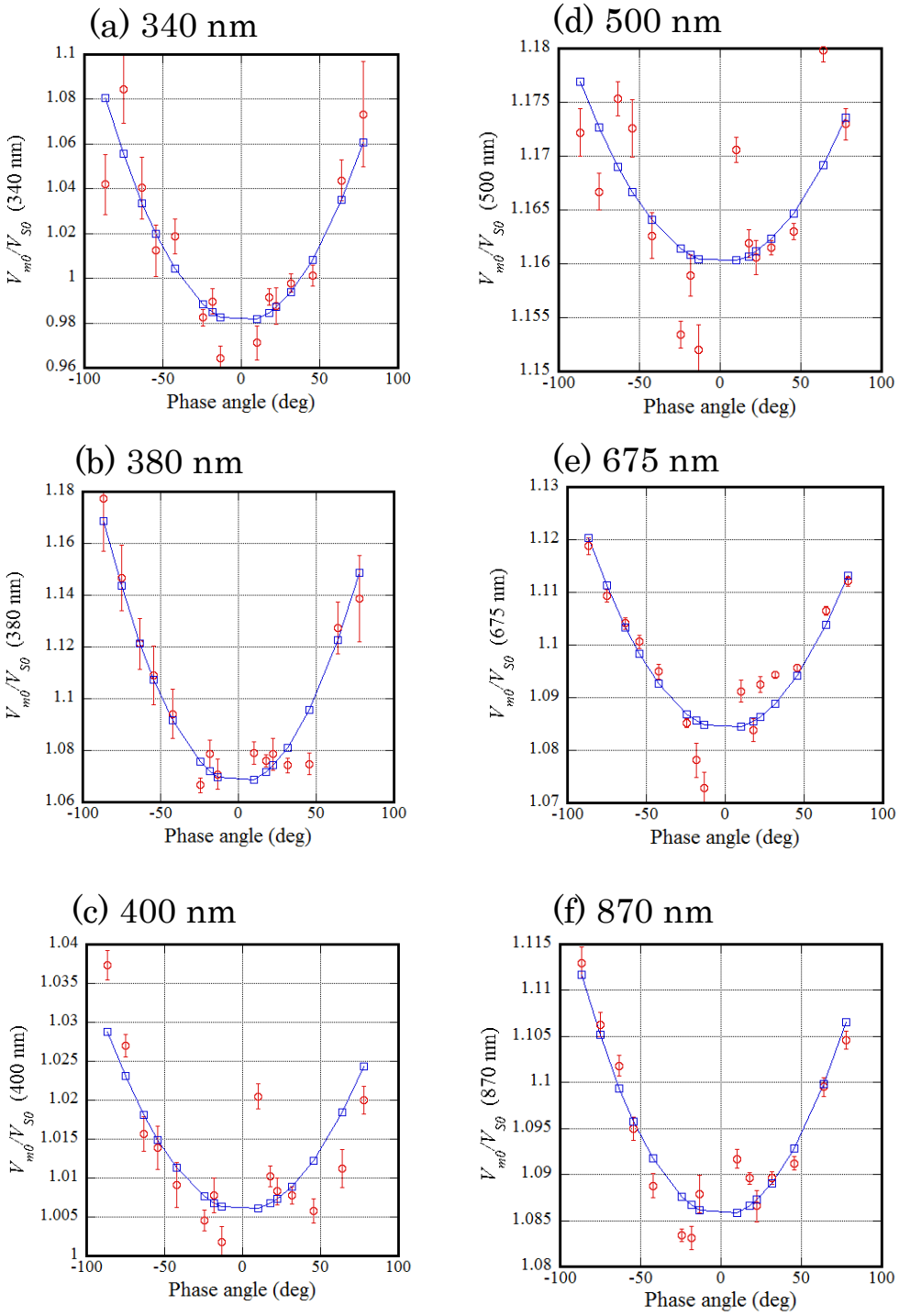

Fig. 5 to be continued.

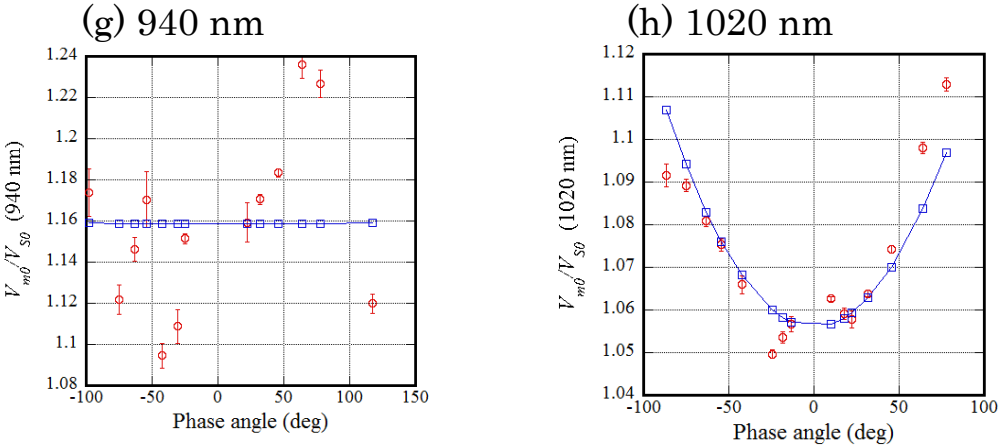

Fig. 5 Relationship between phase angle and reflectance correction factor $C = V_{m\theta} / V_{S\theta}$ in visible and near-infrared region. A regression curve ($C = A_c \cdot g^2 + B_c$, g : phase angle) was also plotted.

to be continued.

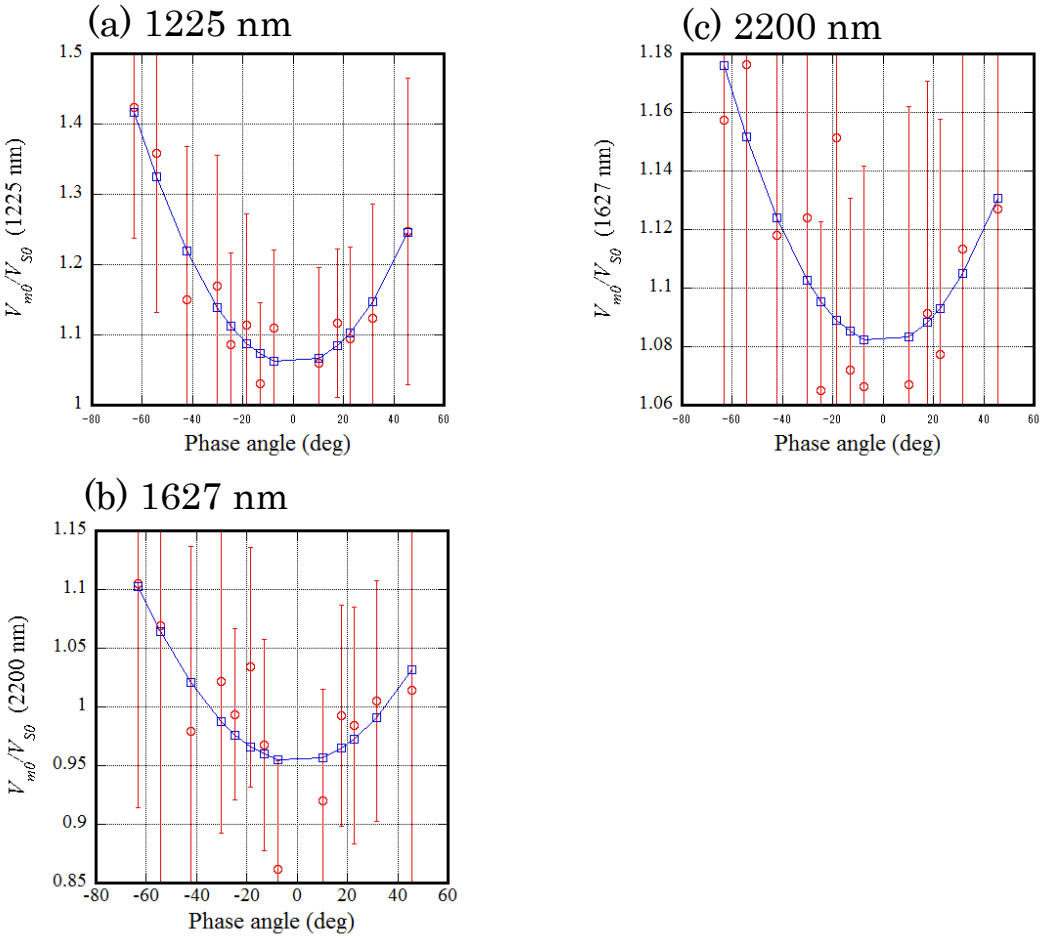

Fig. 6 Relationship between phase angle and reflectance correction factor $C = V_{mθ} / V_{Sθ}$ in shortwave infrared region. A regression curve ($C = A_c \cdot g^2 + B_c$, g : Phase angle) was also plotted.

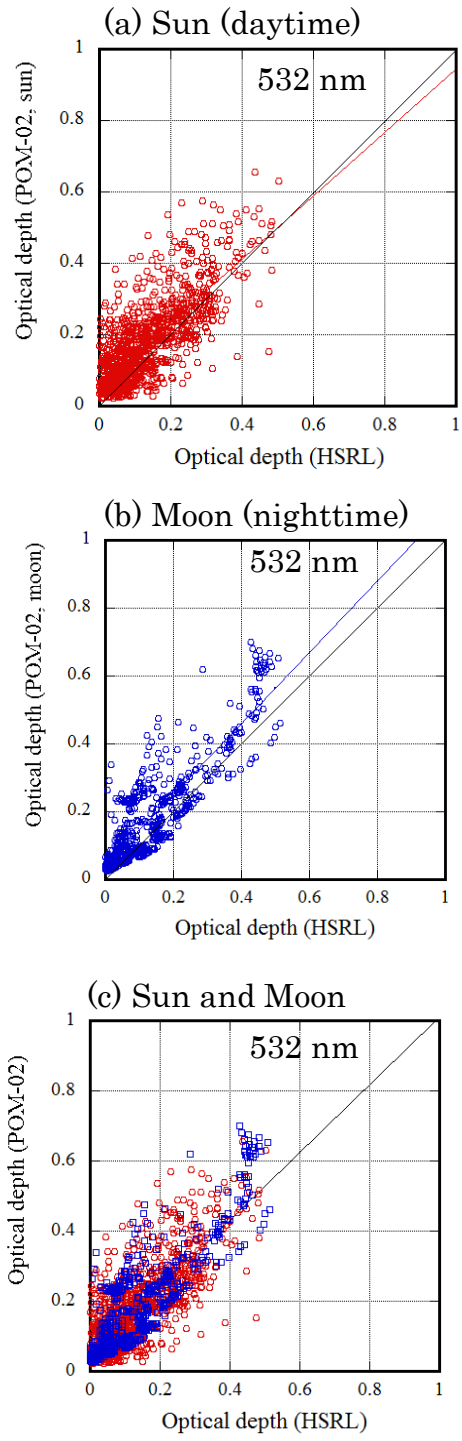

Fig. 7 Scatter plot of NIES/HSRL and POM-02 aerosol optical depth at 532nm. (a) Daytime (red), (b) nighttime (blue), (c) overlapping daytime (red) with nighttime (blue).

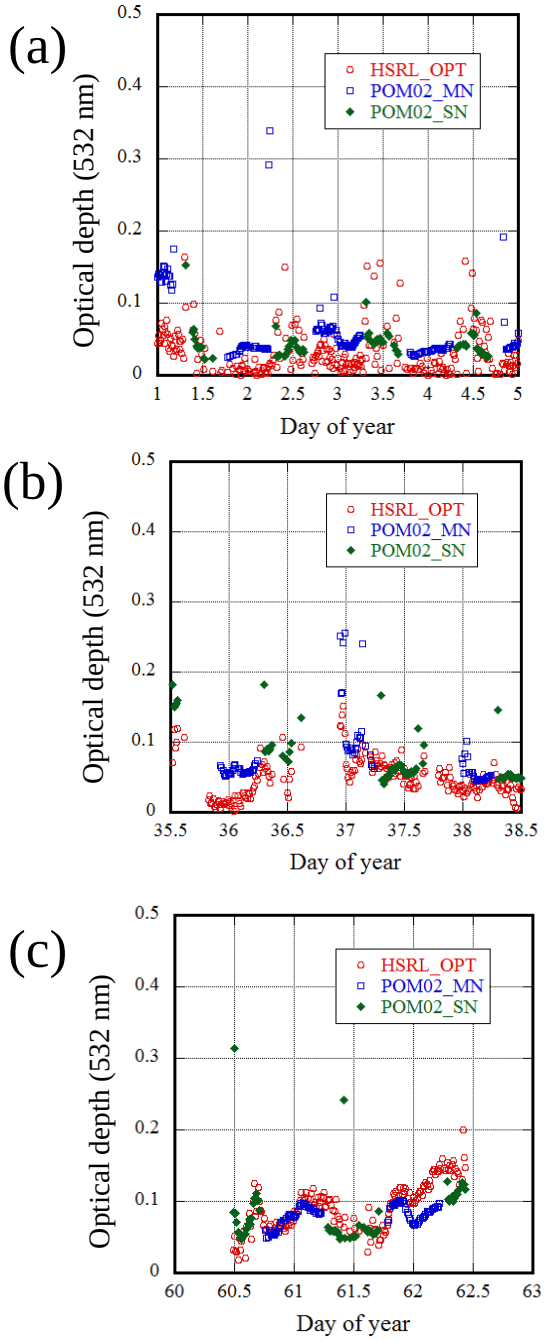

Fig. 8 Examples of time series of NIES/HSRL (red), POM-02 daytime (green), and nighttime (blue) aerosol optical depths at 532 nm. The phase angles (g) during the measurement periods were (a) g = −21.863 to 35.881 degrees, (b) g = 47.454 to 83.190 degrees, and (c) g = −19.150 to 21.573 degrees.

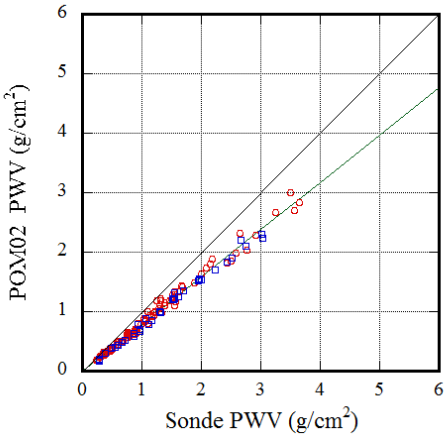

Fig. 9 Scatter plot of radiosonde and POM-02 precipitable water vapor. Daytime (nighttime) measurements are indicated by a red (blue) symbol.

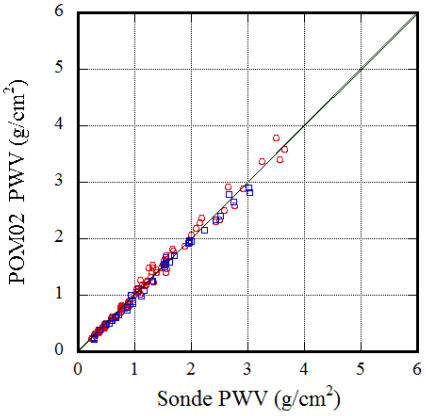

Fig. 10 Same as Fig. 9 except for corrected POM-02 precipitable water vapor.

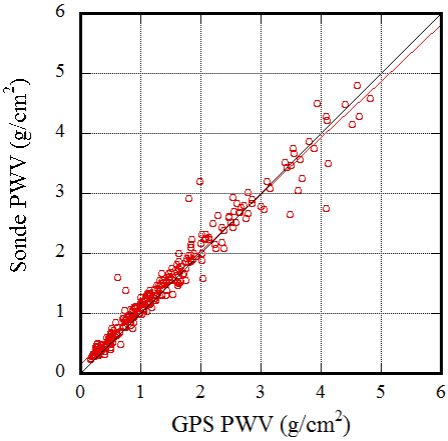

Fig. 11 Scatter plot of GPS and radiosonde precipitable water vapor.

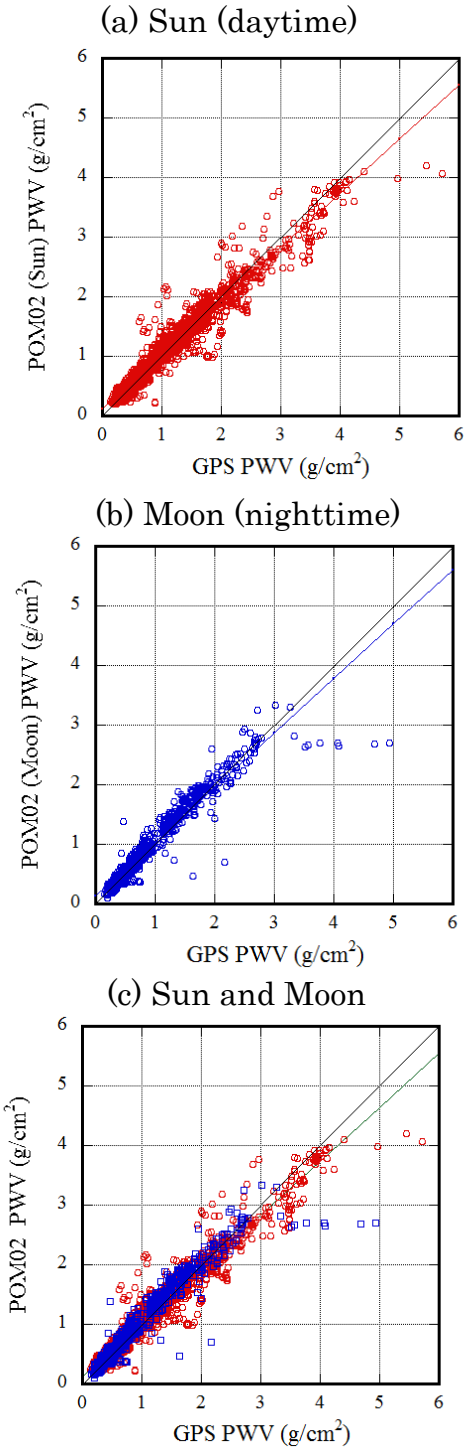

Fig. 12 Scatter plot of PWV from GPS and corrected PWV from POM-02. (a) Daytime (red), (b) nighttime (blue), (c) overlapping daytime (red) with nighttime (blue).

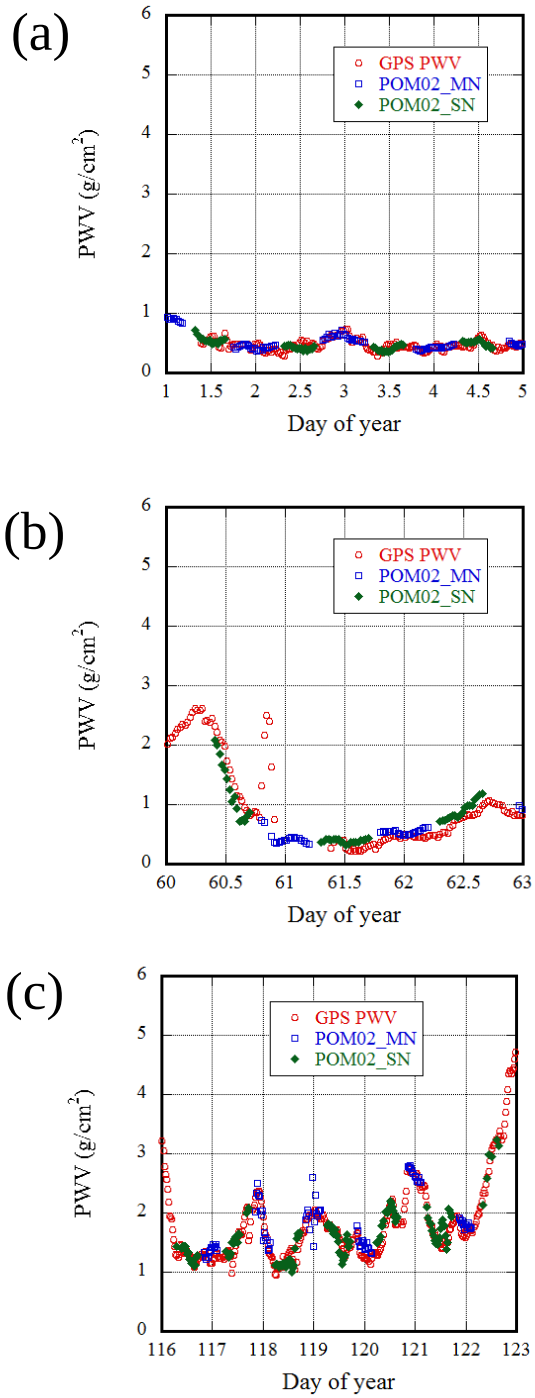

Fig. 13 Examples of time series of GPS (red), POM-02 daytime (green), and nighttime (blue) corrected precipitable water vapor. The phase angles (g) during the measurement periods were (a) g = −21.863 to 35.881 degrees, (b) g = −19.150 to 21.573 degrees, and (c) g = −55.145 to 30.611 degrees.

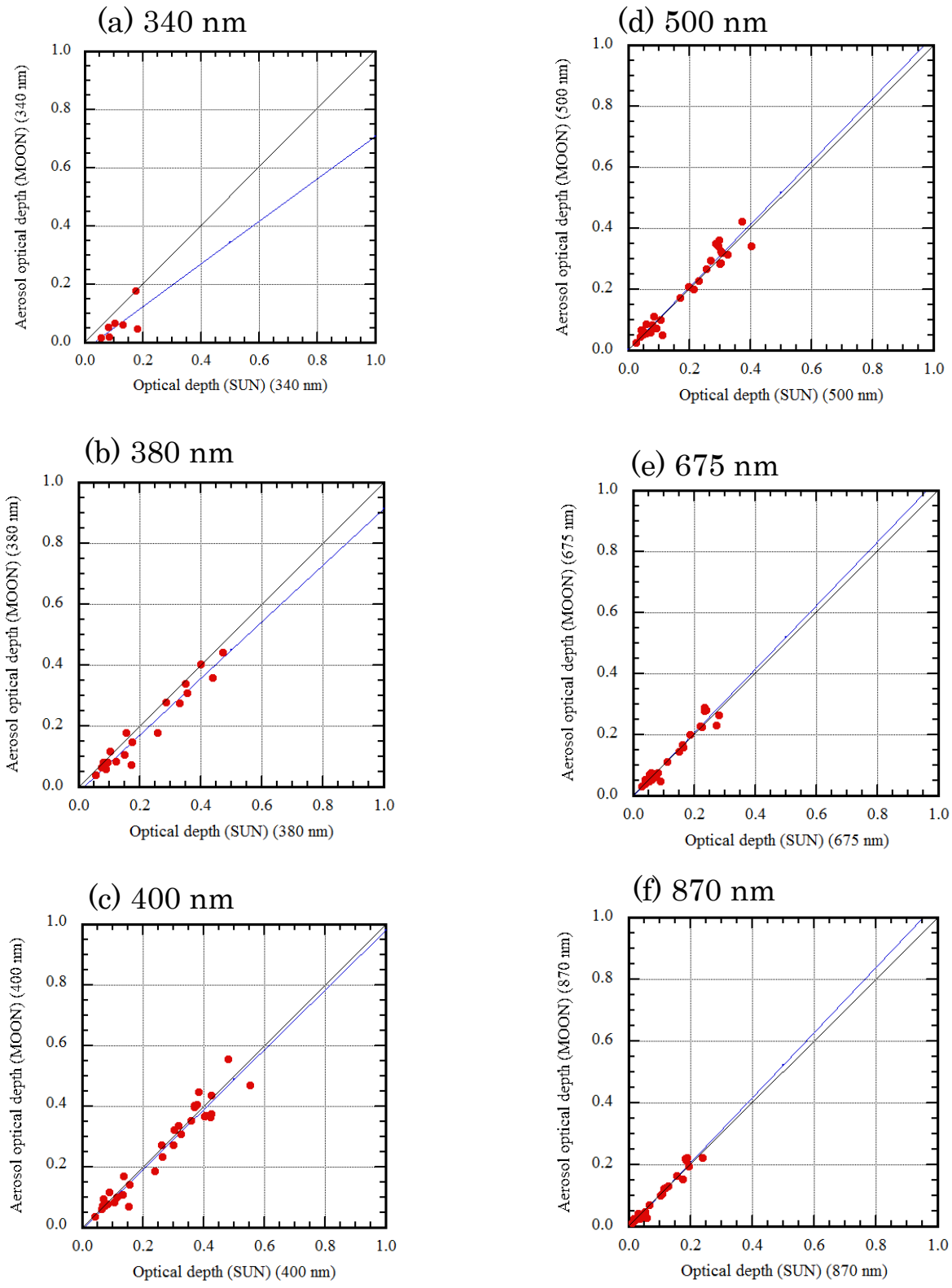

Fig. 14 to be continued.

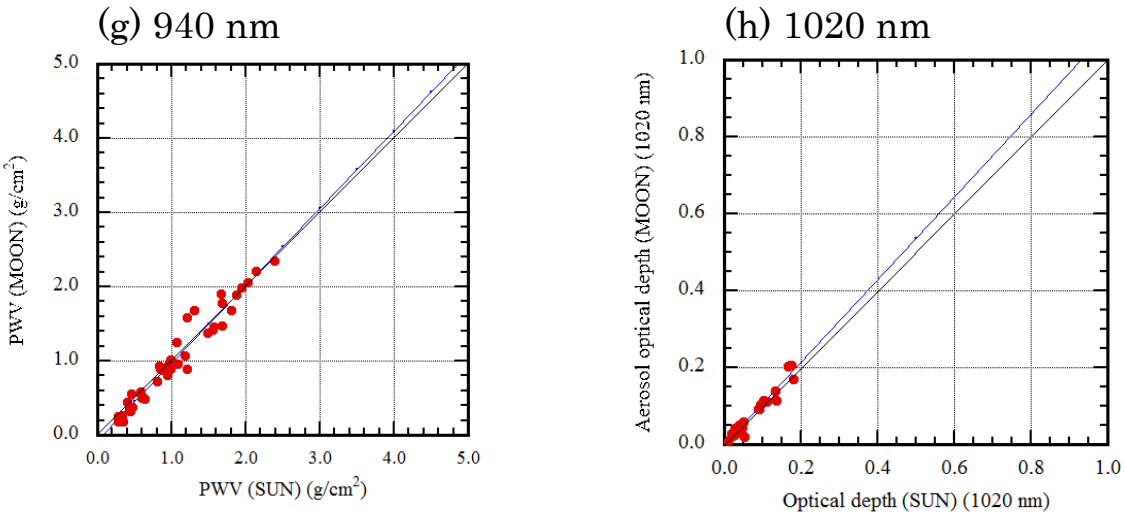

Fig. 14 Scatter plot of the aerosol optical depth (precipitable water vapor) from the sun and the moon. (a) 340 nm AOD, (b) 380 nm AOD, (c) 400 nm AOD, (d) 500 nm AOD, (e) 675 nm AOD, (f) 870 nm AOD, (g) 940nm PWV, (h) 1020 nm AOD.

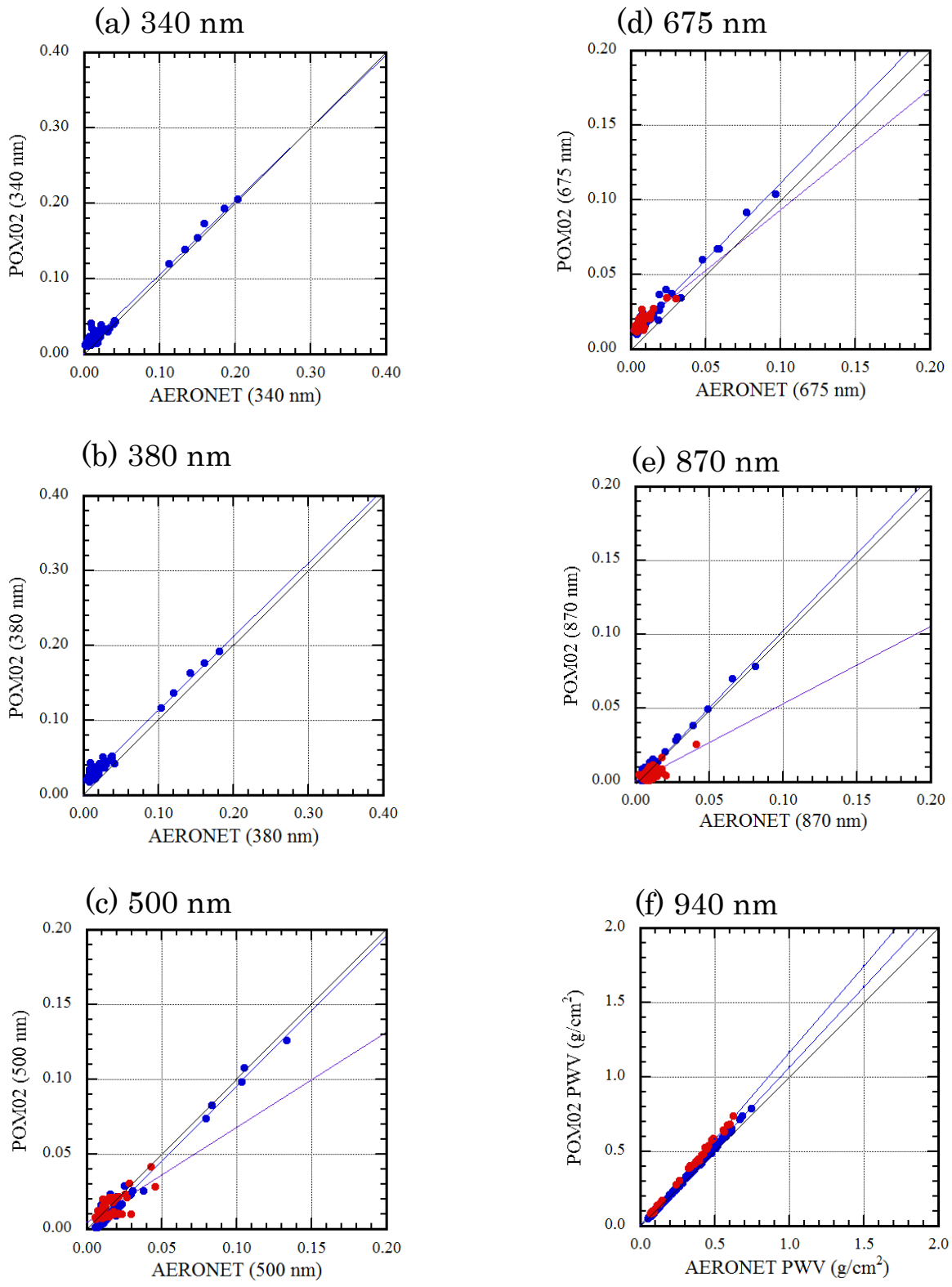

Fig. 15 to be continued.

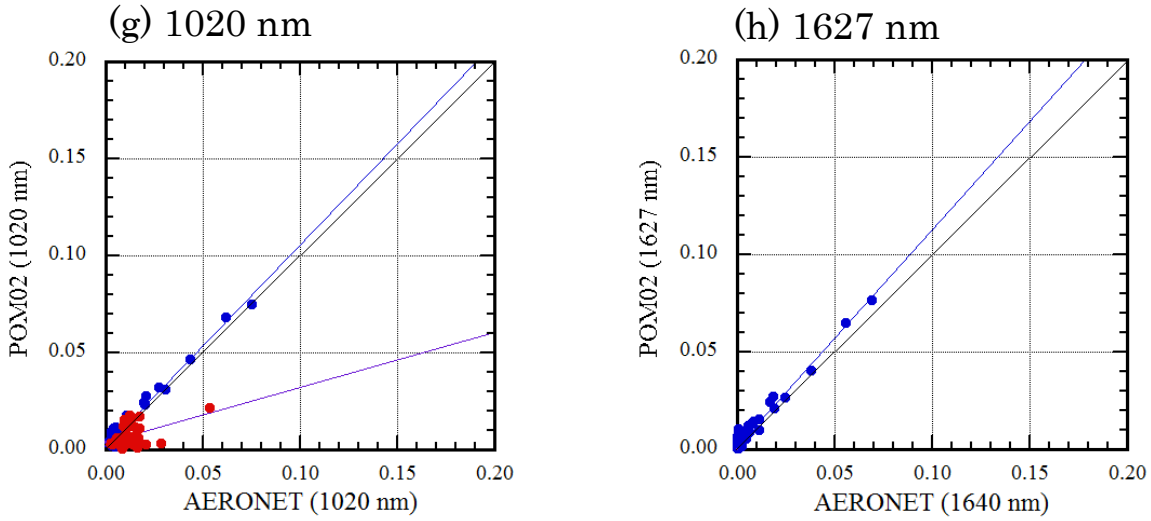

Fig. 15 Scatter plot of AERONET and POM-02 aerosol optical depth (precipitable water vapor). Daytime (nighttime) measurements are indicated by a red (blue) symbol. (a) 340 nm AOD, (b) 380 nm AOD, (c) 500 nm AOD, (d) 675 nm AOD, (e) 870 nm AOD, (f) 940nm PWV, (g)1020nm AOD, (h) 1627 nm AOD.

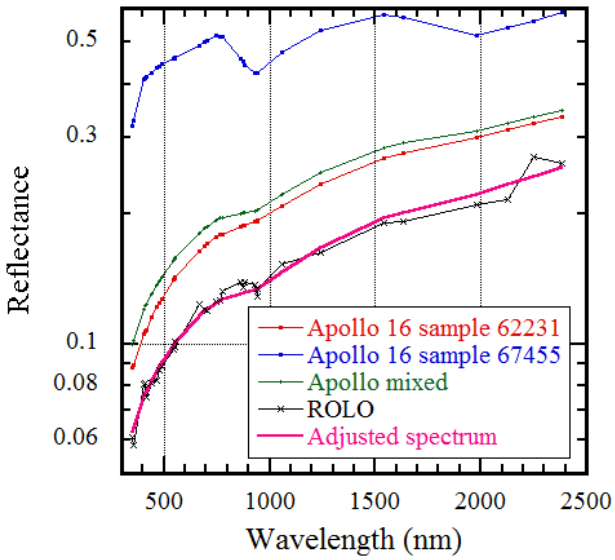

Fig. A1 ROLO smoothed and adjusted reflectance.

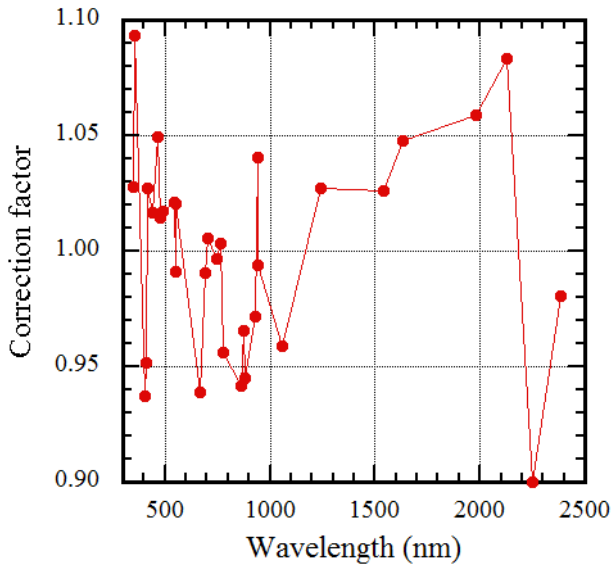

Fig. A2 Coefficients for smoothing at the ROLO 32 wavelength.

Supplement

The time series of the AOD at 500 nm and PWV at Tsukuba for 5 months are shown in Fig. S1 and Fig. S2, respectively. These are non-cloud screened data.
In addition, the time series of the comparison between HSRL and POM-02 AOD and the time series of the comparison between GPS and POM-02 PWV are shown in Fig. S3 and Fig. S4.

Figure captions

Fig. S1 Time series of the AOD at 500 nm at Tsukuba for 5 months. (a) January, (b) February, (c) March, (d) April, (e) May.

Fig. S2 Time series of the PWV at Tsukuba for 5 months. (a) January, (b) February, (c) March, (d) April, (e) May.

Fig. S3 Time series of the comparison between HSRL and POM-02 AOD for 5 months. Red symbols are HSRL AOD, blue symbols are AOD in the nighttime, and green symbols are AOD in the daytime. The data are 15-minute averages.

Fig. S4 Time series of the comparison between GPS and POM-02 PWV for 5 months. Red symbols are GPS PWV, blue symbols are PWV in the nighttime, and green symbols are PWV in the daytime. The data are 30-minute averages.

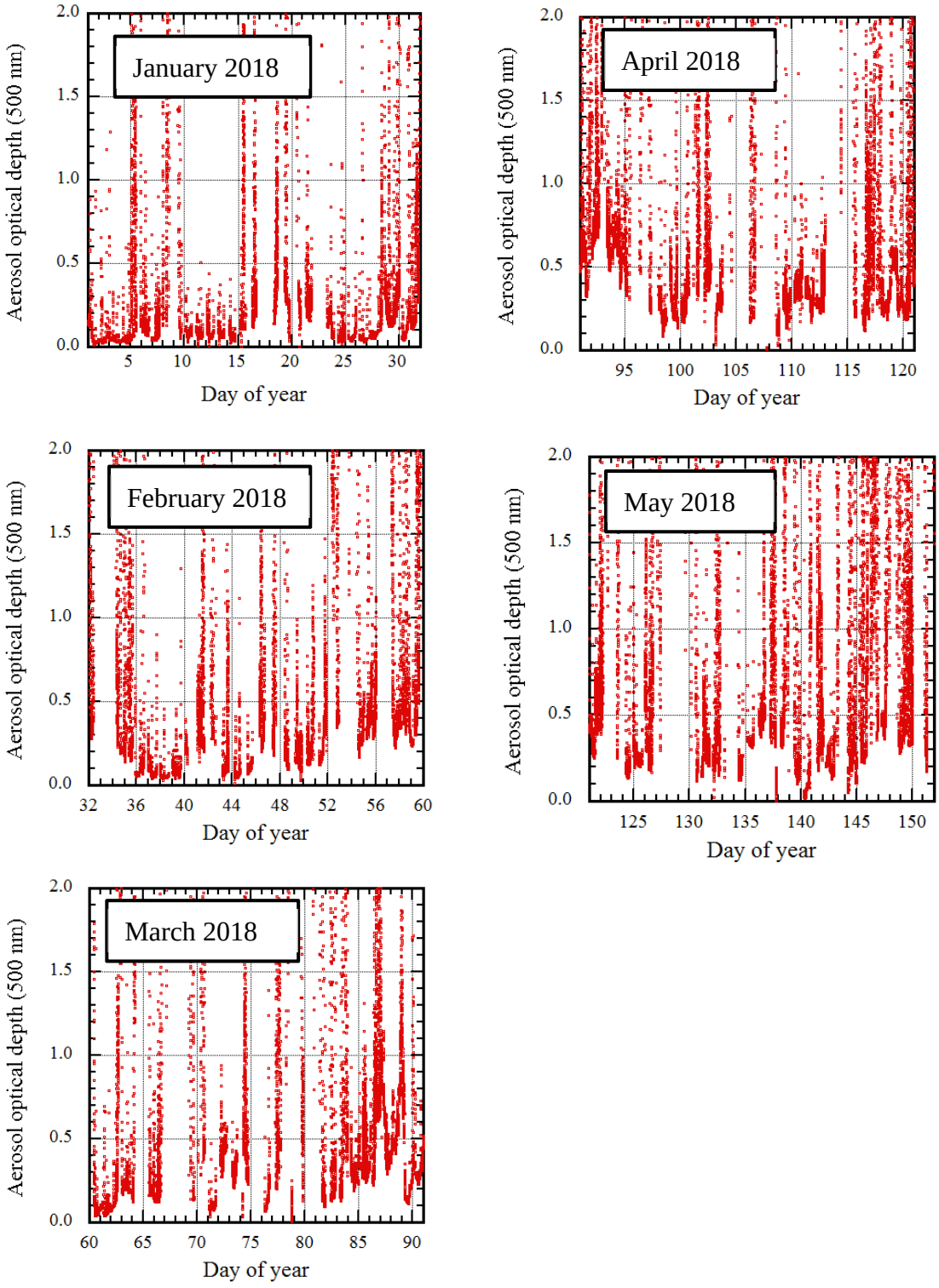

Fig. S1 Time series of the AOD at 500 nm at Tsukuba for 5 months.
(a) January, (b) February, (c) March, (d) April, (e) May.

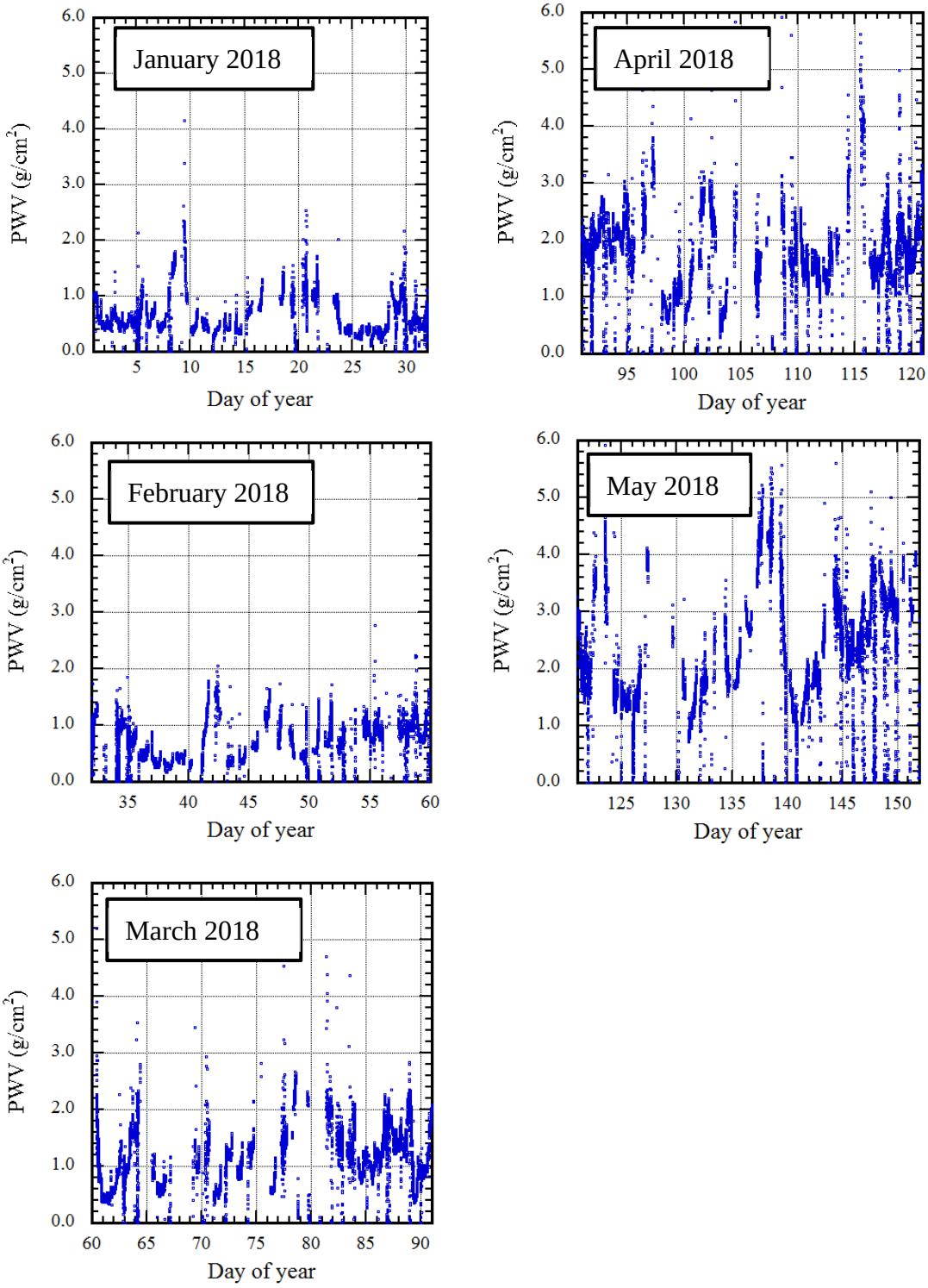

Fig. S2 Time series of the PWV at Tsukuba for 5 months.
(a) January, (b) February, (c) March, (d) April, (e) May.

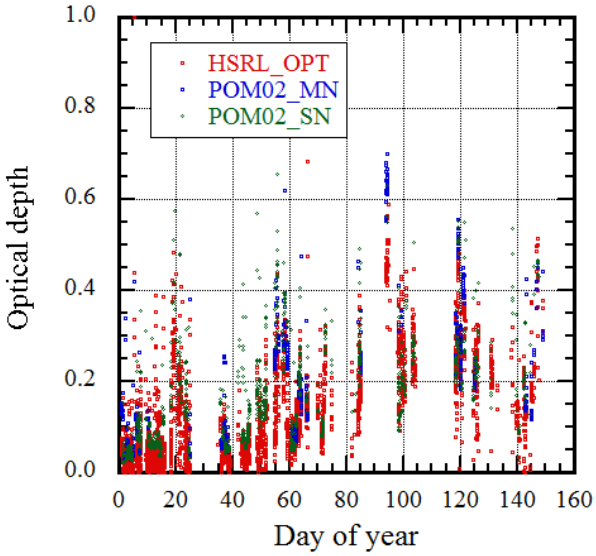

Fig. S3 Time series of the comparison between HSRL and POM-02 AOD. Red symbols are HSRL AOD, blue symbols are AOD in the nighttime, and green symbols are AOD in the daytime. The data are 15-minute averages.

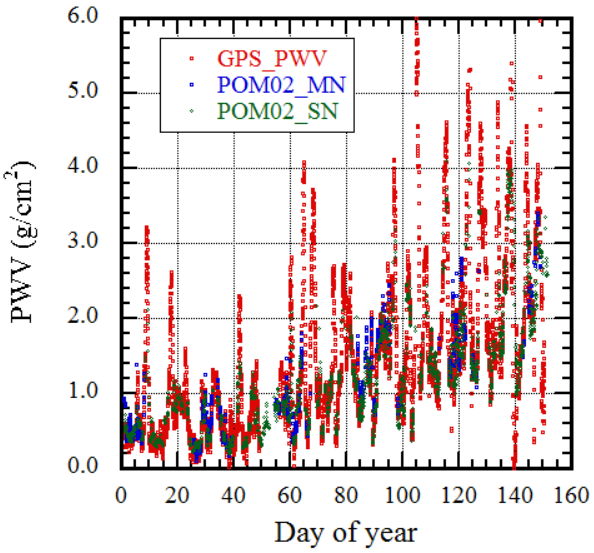

Fig. S4 Time series of the comparison between GPS and POM-02 PWV. Red symbols are GPS PWV, blue symbols are PWV in the nighttime, and green symbols are PWV in the daytime. The data are 30-minutes averages.